Quaternium-22 as a High-Performance Corrosion Inhibitor for Carbon Steel in Acidic Media: Experimental and Theoretical Insights

Mohammed Afifi , Nasser Elbasiony , Aziza S. El-Tabei , Shimaa Abdel Halim , Magdy A. M. Ibrahim *

Posted Date: 27 February 2026

doi: 10.20944/preprints202602.1773.v1

Keywords: corrosion inhibition; carbon steel; quaternium-22 surfactant; green corrosion inhibitors; impedance spectroscopy; polarization; DFT; molecular dynamics

 doi:10.20944/preprints202602.1773.v1

Article

Quaternium-22 as a High-Performance Corrosion Inhibitor for Carbon Steel in Acidic Media: Experimental and Theoretical Insights

Mohammed Afifi [1], Nasser elbasiony [2], Aziza S. El-Tabei [2], Shimaa Abdel Halim [3] and Magdy A. M. Ibrahim [1,*]

[1] Department of Chemistry, Faculty of Science, Ain Shams University, Abbassia, Cairo 11566 and Egypt

[2] Egyptian Petroleum Research Institute, Nasr City, Cairo 11727, Egypt

[3] Department of Chemistry, Faculty of Education, Ain Shams University, Roxy, Cairo 11711, Egypt

* Correspondence: magdyibrahim@sci.asu.edu.eg; Tel.: (00201149590687)

Abstract

This work provides an integrated experimental and computational assessment of the cationic surfactant Quaternium-22 (Q-22) as a potentially eco-compatible corrosion inhibitor for carbon steel (CS) in 1 M hydrochloric acid. Gravimetric analysis and electrochemical techniques: electrochemical impedance spectroscopy (EIS) and potentiodynamic polarization (PDP) were employed over a 20–50 °C temperature range. Q-22 exhibited mixed-type inhibition behavior, with efficiency rising to 97% at an optimal concentration of 277 μmol L^{-1}. Performance was concentration-dependent but diminished with increasing temperature, indicating partial inhibitor desorption at elevated temperatures. Thermodynamic evaluation confirmed a spontaneous adsorption process aligned with the Langmuir isotherm, involving a mixed physisorption and chemisorption mechanism. Surface characterization via scanning electron microscopy (SEM), atomic force microscopy (AFM), contact angle (CA) measurement, and X-ray photoelectron spectroscopy (XPS) verified the formation of a coherent, hydrophobic inhibitor layer that substantially reduced surface roughness and corrosion damage. Theoretical validation using density functional theory (DFT), natural bond orbital (NBO) analysis, and molecular dynamics (MD) simulations revealed strong adsorption energetics and favorable electronic properties consistent with the inhibitor's high experimental efficacy. The collective findings establish Q-22 as a potent, eco-compatible corrosion inhibitor for CS in acidic environments, operating through a robust adsorptive film-forming mechanism.

Keywords: corrosion inhibition; carbon steel; quaternium-22 surfactant; green corrosion inhibitors; impedance spectroscopy; polarization; DFT; molecular dynamics

1. Introduction

The corrosion of metals and alloys represents a pervasive and costly global challenge, with profound implications for industrial safety, economic stability, and environmental integrity [1, 2]. Over $2.5 trillion is spent on corrosion worldwide each year, much of which can be avoided with effective management techniques [3]. Nowhere is this more evident than in the petroleum industry, where aggressive environments, characterized by the presence of acids, brines, and corrosive gases, relentlessly attack infrastructure. Carbon steel (CS), the workhorse material for pipelines, tanks, and reactors due to its mechanical strength and cost-effectiveness, is highly susceptible to degradation, particularly in acidic media used for pickling, descaling, and oil well acidizing [4, 5]. The transfer of crude oil, which often contains corrosive species like chlorides, carbon dioxide, and hydrogen sulfide, accelerates this degradation, leading to equipment failure, production downtime, environmental contamination, and substantial financial losses [6].

 doi:10.20944/preprints202602.1773.v1

Within the suite of corrosion mitigation strategies, such as protective coatings, cathodic protection, and alloy selection, the application of corrosion inhibitors stands out as a particularly efficient and cost-effective approach, especially for enclosed systems and acidic media [7,8]. These compounds function by introducing a small concentration of chemical species into the aggressive environment. An effective inhibitor adsorbs onto the metal substrate, forming a protective interfacial layer that significantly retards the corrosion rate [9]. In this context, organic molecules featuring heteroatoms (e.g., N, O, S), π-electron systems, and polar functional groups have emerged as highly promising candidates. Their efficacy predominantly stems from their strong adsorption affinity for metal surfaces. Upon adsorption, these molecules block electrochemically active sites and create a physical barrier that isolates the metal from the corrosive electrolyte [10–12].

The amphiphilic structure of surfactants, which consists of a hydrophilic head group coupled with a hydrophobic tail, makes them an effective class of organic corrosion inhibitors [13]. While the hydrophobic tail creates a water-repellent barrier that prevents corrosive species from entering acidic media, the hydrophilic head—typically a quaternary ammonium group in cationic surfactants—promotes electrostatic adsorption onto the metal surface [14]. Molecular characteristics like chain length, head group type, and the presence of specific functional groups that increase adsorption strength have a significant impact on the inhibition efficiency [15].

Driven by growing environmental and health concerns, the field of corrosion science is increasingly shifting towards "green" or eco-friendly inhibitors [16,17]. These are characterized by low toxicity, reported biodegradability, and relatively well-documented toxicological profiles. While many traditional inhibitors are effective, their ecological unfriendliness has spurred the search for safer alternatives. In this context, quaternary ammonium compounds (Quats), which are widely used as biocides and disinfectants, are being re-evaluated for their corrosion inhibition potential. Their inherent biodegradability and well-understood toxicological profiles make them attractive candidates for developing effective yet environmentally acceptable inhibitors [18,19].

Quaternium-22 (Q-22), chemically defined as N-(2-hydroxyethyl)-N, N-dimethyl-3-(gluconoylamino)propanaminium chloride, is a cationic surfactant that fits this profile of potentially less hazardous inhibitor. Its molecular structure ($C_{13}H_{29}ClN_2O_7$) is particularly noteworthy, as it integrates multiple functional groups synergistic to corrosion inhibition within a single molecule: a quaternary ammonium center (N^+) for strong electrostatic/physisorption to the negatively charged steel surface, a hydrophobic alkyl chain for surface coverage, multiple ether and hydroxyl groups (-O-) from the gluconate moiety for potential chemisorption via lone-pair electrons, and an amide linkage (-NH-CO-) for additional anchoring points [20]. This unique architecture, combining a cationic head with a polar, hydroxy-rich tail, is hypothesized to have a multi-modal adsorption mechanism that could lead to superior inhibition efficiency and film stability. The gluconate moiety is itself known to be benign and biodegradable, enhancing the compound's green credentials [21].

However, despite its commercial availability and multi-functional structure, the corrosion inhibition mechanism of Quaternium-22 for CS in acidic media remains inadequately understood, mostly concerning the synergistic roles of its quaternary ammonium and polyhydroxy gluconate moieties. Therefore, this study addresses this gap through a comprehensive evaluation of Quaternium-22 as an efficient and environmentally acceptable corrosion inhibitor for CS in 1.0 M HCl. Inhibition performance and mechanism were evaluated using gravimetric and electrochemical techniques, complemented by thermodynamic and adsorption analyses. Its mixed adsorption mode and high efficiency at low concentrations were explained mechanistically by using surface characterization and multiscale computational insights to further correlate molecule structure with inhibitory activity.

 doi:10.20944/preprints202602.1773.v1

2. Materials and Methods

2.1. Materials

ASTM Grade A35 carbon steel, which is commonly used in industrial settings, was used to prepare the working electrode. **Table 1** describes its chemical composition as verified by optical emission spectrometry. Before each experiment, coupons were mechanically abraded with increasing grades of silicon carbide paper (up to 1200 grit), ultrasonically cleaned in acetone for 10 minutes, thoroughly rinsed with double-distilled water, and dried under a warm air stream to ensure a reproducible surface condition.

Table 1. Chemical composition of carbon steel.

Elements	Carbon (C)	Silicon (Si)	Manganese (Mn)	Sulfur (S)	Copper (Cu)	Iron (Fe)
Content (wt.%)	0.26	0.28	1.05	0.003	0.2	Balance

2.2. Inhibitor and Solution Preparation

The corrosion inhibitor, Quaternium-22 (Q-22), was acquired from UFC Bio-technology Co., Ltd, USA. Q-22 is a cationic surfactant recognized for its eco-friendly profile, commonly used in cosmetic and antistatic formulations. Its molecular structure, IUPAC name, chemical formula, and molecular weight are detailed in Table 2. An exact amount of Q-22 was dissolved in 1.0 M hydrochloric acid (HCl) to create a stock solution (1.0×10^{-2} M). This stock was then diluted with the 1.0 M HCl electrolyte to generate all functioning inhibitor solutions. Analytical-grade concentrated HCl (BDH) was diluted with double-distilled water to create an aggressive electrolyte, 1.0 M HCl.

Table 2. Structure formula of the used inhibitor.

Organic Compound	
Quaternium-22 (Q-22)	
Structure	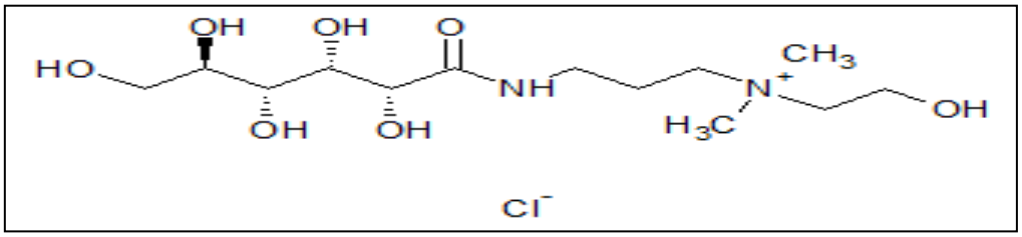
IUPAC Name &Chemical Formula	N-(2-hydroxyethyl)-N, N-dimethyl-3-(gluconoylamino)propanaminium chloride $C_{13}H_{29}N_2ClO_7$
Molecular Weight	360.83 g/mol

2.3. Gravimetric (Weight Loss) Measurements

Gravimetric measurements were conducted to quantitatively assess the corrosion rate and inhibition efficiency of Q-22 over time. The tests were performed in a 250 mL glass vessel with an inner diameter of 6 cm, containing 100 mL of the test solution (1.0 M HCl with and without inhibitor) and maintained at 25 ± 1 °C. CS coupons, with dimensions of 2.0 × 2.0 × 0.1 cm, were prepared by sequential abrasion with successive grades of silicon carbide paper (from coarse to 1200 grit),

 doi:10.20944/preprints202602.1773.v1

followed by ultrasonic cleaning in acetone for 10 minutes, rinsing with double-distilled water, and thorough drying before being accurately weighed.

Each coupon was suspended approximately 1 cm below the solution surface using a glass hook. After a specified immersion period (e.g., 6 hours), the coupons were removed, carefully rinsed with double-distilled water to remove loose corrosion products, dried, and re-weighed. The experiment was performed in triplicate for each condition to ensure reproducibility, and the average weight loss was used for all calculations.

The average weight loss (ΔW), corrosion rate (CR), and inhibition efficiency ($IE\%$) were calculated as follows:

The weight loss for each coupon was determined using:

$$W_o = W_B - W_A \quad \textbf{(1)}$$

where:

W_o = weight of metal loss in the corrosive solution

W_B = weight of metal before exposure to the corrosive solution

W_A = weight of metal after exposure to the corrosive solution

The corrosion rate (CR) was then calculated from the average weight loss:

$$\text{Corrosion rate (mpy)} = \frac{K \Delta W}{\rho A t} \quad \textbf{(2)}$$

where:

K is a constant (8.76×10^4 for the rate in mpy),

A is the total surface area of the coupon (cm^2),

t is the immersion time (hours),

ϱ is the density of the CS ($g\ cm^{-3}$).

The surface coverage (θ) and inhibition efficiency ($IE\%$) were determined as:

$$\theta = \frac{\Delta W_0 - \Delta W_{inh}}{\Delta W_0} \quad \textbf{(3)}$$

$$\text{IE}\ \% = \ \theta \ \times 100 = \frac{W_0 - W_{inh}}{W_0} \times 100\% \quad \textbf{(4)}$$

where:

ΔW_0 and ΔW_{inh} are the average weight losses for the blank and inhibited solutions.

2.4. Studies on Electrochemistry

A Gamry Reference 3000™ potentiostat/galvanostat/ZRA was used to perform electrochemical experiments. A typical double-jacketed glass cell with three electrodes was used. The CS rod with a 0.5 cm^2 exposed geometric area was used as the working electrode; a graphite rod was used as the counter electrode; and a saturated calomel electrode (SCE) was used as the reference. A 1.0 M HCl solution with and without different doses of the Q-22 inhibitor (41, 69, 138, and 277 μmol L^{-1}) served as the electrolyte. A Julabo thermostatic water circulator was used to keep the cell temperature at the specified level (20, 30, 40, or 50 °C). The working electrode was submerged before every test until a stable open-circuit potential (OCP) was reached, which usually took 20 minutes.

At the OCP, electrochemical impedance spectroscopy (EIS) was carried out using a sinusoidal potential perturbation with an amplitude of 10 mV RMS throughout a frequency range of 100 kHz to 0.1 Hz (10 points per decade). Following the EIS measurements, Potentiodynamic Polarization (PDP) scans were obtained. With a scan rate of 0.167 mV s^{-1}, the potential was swept from -250 mV to +250 mV vs. OCP. To guarantee reproducibility, each experiment was carried out three times. Each experiment was repeated three times.

2.5. Surface Characterization

Surface characterization was conducted to provide direct visual, topographical, and chemical evidence for the protective film formation indicated by the electrochemical and gravimetric data. The

 doi:10.20944/preprints202602.1773.v1

CS specimens were examined after 24 hours of immersion in 1.0 M HCl, both in the absence (blank) and presence of the optimal concentration of Q-22. Identical sample preparation protocols were followed for all analyses to ensure a direct and consistent comparison.

2.5.1. X-Ray Photoelectron Spectroscopy (XPS):

Surface chemical analysis was conducted via X-ray photoelectron spectroscopy (XPS) using a Kratos Axis Ultra DLD spectrometer. This technique was employed to identify the elemental composition and chemical bonding states, specifically to verify the adsorption of the Q-22 inhibitor on the CS surface.

2.5.2. SEM and AFM

The surface morphological and chemical composition of the CS specimens were examined after 24 hours of immersion in 1.0 M HCl solution, both without inhibitor (blank) and with the optimal concentration of Q-22. The analysis was performed to visually corroborate the protective film formation indicated by the electrochemical and weight-loss data. High-resolution micrographs were obtained using a Field Emission Scanning Electron Microscope (FE-SEM, NOVA NANOSEM 450, FEI, USA). Furthermore, the surface topography and roughness at the nanoscale were quantitatively assessed using an Atomic Force Microscope (AFM, MFP-3D, Asylum Research, USA) operating in tapping mode.

2.5.3. Surface Wettability (Contact Angle) Measurements:

Surface wettability, an indicator of hydrophobicity, was evaluated using an automatic tensiometer (Easy Drop D04010, KRÜSS GmbH, Germany) at 20 °C. The static water contact angle was measured to quantify the change in surface hydrophobicity induced by the inhibitor film.

2.6. Quantum Chemical Studies

2.6.1. Theoretical Computations

Density Functional Theory (DFT) calculations were performed to determine the molecular parameters of Q-22. Structural visualization and vibrational frequency analyses were carried out using GaussView 5.0.9. At the same time, all quantum chemical calculations were conducted with the B3LYP hybrid functional and the 6–311++G(d,p) basis set using the Gaussian 09 package [22]. Global reactivity descriptors, including E_{HOMO}, E_{LUMO}, energy gap (ΔE), dipole moment (μ), ionization potential (I), electron affinity (χ), electronegativity (ϕ), chemical hardness (ψ), softness (S), electrophilicity (ω), nucleophilicity (ε), electro-accepting (ω^{+}) and electro-donating (ω^{-}) powers, back-donation energy (ΔE), fraction of electron transfer (ΔN), and inhibitor–metal interaction energy ($\Delta E_{Fe/Q-22}$), were calculated. Local reactivity was evaluated using Fukui functions [23–25], while Natural Bond Orbital (NBO) analysis was employed to examine charge distribution, orbital interactions, and their influence on molecular stability.

2.6.2. Molecular Simulation (MD) Dynamics

The adsorption behavior of Q-22 on the Fe (111) surface was investigated using molecular dynamics (MD) simulations. The metal surface was modeled as a solvent-free vacuum slab under periodic boundary conditions, with a ten-layer Fe (111) supercell and a 30 Å vacuum to prevent interactions between periodic images (simulation box: 24.32 × 24.32 × 9.10 $Å^3$). After energy minimization of both the Q-22 molecule and the Fe surface, the inhibitor was adsorbed, and simulations were performed using the COMPASS force field within the Discover module. Adsorption strength was evaluated through interaction and binding energies, while radial distribution function (RDF) analysis was applied to characterize the nature of Q-22–Fe interactions.

 doi:10.20944/preprints202602.1773.v1

2.6.3. NBO Analysis

The intra- and intermolecular interactions of Q-22 were examined using Natural Bond Orbital (NBO) analysis, specifically donor-acceptor interactions between filled (bonding or lone-pair) and empty (antibonding) orbitals. Second-order perturbation theory was used to determine the stabilization energies of these interactions:

$$E^{(2)} = \Delta E_{ij} = q_i \, (F \, (ij) \, 2 \, / \varepsilon_j - \varepsilon_i) \quad \textbf{(5)}$$

where q_i is the occupancy of the donor orbital, F_{ij} is the off-diagonal Fock matrix element, and ϵ_i and ϵ_j are the orbital energies of the donor and acceptor, respectively. This analysis provides insight into the electron delocalization and the strength of interactions that govern Q-22 adsorption on the steel surface.

3. Results and Discussion

3.1. Gravimetric (Weight Loss) Measurements

The corrosion behavior of CS in 1.0 M HCl solution, in the absence and presence of varying concentrations of Q-22, was assessed using the weight loss technique. As depicted in **Figure 1**, the mass loss of CS specimens decreases progressively with increasing concentrations of Q-22, demonstrating the inhibitor's effectiveness in retarding metal dissolution. This decline in weight loss reflects the ability of Q-22 molecules to adsorb onto the steel surface, thereby limiting the active sites available for the corrosion reaction and forming a protective barrier against the acidic medium.

The linear correlation observed between weight loss and immersion time for both inhibited and uninhibited systems suggests that the corrosion process proceeds uniformly and that no insoluble corrosion products accumulate on the surface during immersion. In such cases, inhibition occurs primarily through the adsorption of inhibitor molecules on the metal surface. These adsorbed species can either physically block anodic and cathodic reaction sites or modify the kinetics of the charge-transfer reactions occurring at the interface.

Data presented in **Table 3** for surface coverage (θ) and inhibition efficiency (IE%) indicate that the fraction of the surface covered by the inhibitor increases with rising inhibitor concentration, and consequently, the inhibition efficiency (IE%) shows a corresponding enhancement.

As the Q-22 concentration increases from 41 to 277 μmol L^{-1}, the corrosion rate decreases markedly, while inhibition efficiency enhances significantly. This trend is attributed to the cationic surfactant nature of Q-22, which promotes molecular adsorption through electrostatic interactions between the positively charged quaternary ammonium headgroups and the negatively charged steel surface. Additionally, the polar functional groups and hydrophilic moieties of Q-22 facilitate stronger anchoring and more homogeneous surface film formation. The adsorbed inhibitor film minimizes metal dissolution by blocking electrolyte access and suppressing both anodic and cathodic reactions [26].

Overall, the gravimetric results confirm that adsorption at the metal–solution interface is the predominant mechanism of corrosion inhibition, with efficiency directly linked to the degree of surface coverage by Q-22 molecules.

Table 3. Surface coverage (θ) and inhibition efficiency (IE%) for CS in 1.0 M HCl at 20 °C as a function of immersion time and varying concentrations of Q-22 inhibitor.

Conc. (μmol L^{-1})	**Surface Coverage (θ)**

 doi:10.20944/preprints202602.1773.v1

t (min)	30	60	90	120	150	180
Blank	-	-	-	-	-	-
41	0.7985	0.7972	0.7675	0.7259	0.7175	0.7062
69	0.8917	0.8797	0.8770	0.8614	0.8472	0.8436
138	0.9477	0.9209	0.9108	0.9006	0.8997	0.8981
277	0.9552	0.9450	0.9394	0.9367	0.9308	0.9299
	Inhibition efficiency (%*IE*)					
Blank	-	-	-	-	-	-
41	79.85	79.72	76.75	72.59	71.75	70.61
69	89.17	87.97	87.70	86.14	84.72	84.36
138	94.77	92.09	91.08	90.06	89.97	89.81
277	95.52	94.50	93.94	93.67	93.08	92.99

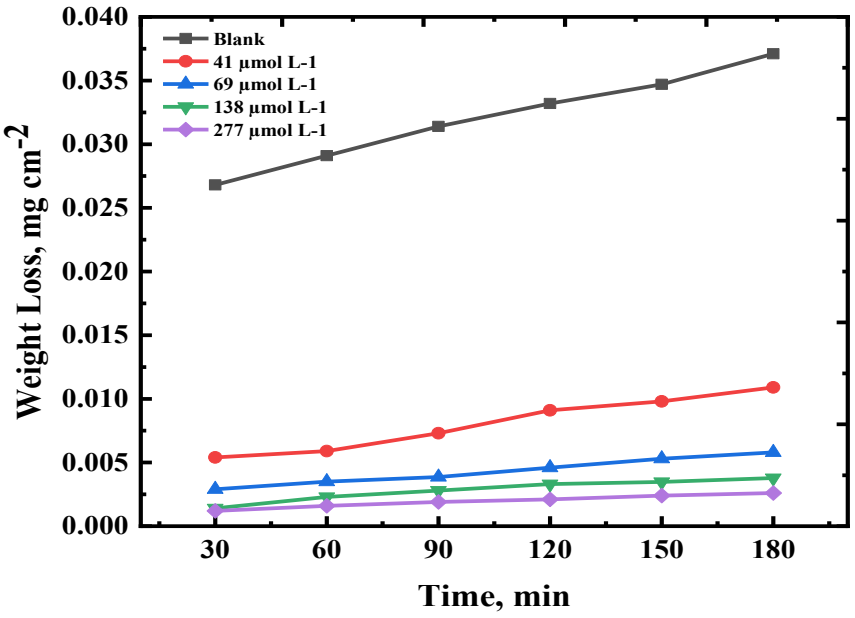

Figure 1. Weight loss versus time for CS in 1.0 M HCl without and with different Q-22 concentrations at 20 °C.

3.2. Electrochemical Measurements

3.2.1. Electrochemical Impedance Spectroscopy (EIS) Measurements

Nyquist and Bode plots for CS in the absence and presence of various Q-22 concentrations (41 - 277 µmol L^{-1}) at temperatures ranging from 20 to 50 °C are presented in **Figure 2 and Figure 3.** The Nyquist plots (**Figures 2a, 2b, 2c & 2d**) consistently display a single, depressed capacitive loop, the diameter of which increases significantly with increasing Q-22 concentration. The depression of the semicircle, a common feature attributed to surface inhomogeneity and roughness [27], was accounted

 doi:10.20944/preprints202602.1773.v1

for in the analysis by replacing an ideal capacitor with a constant phase element (CPE). The impedance spectra consistently feature a prominent capacitive loop, accompanied by a low-frequency inductive dispersion (inductive arc). This inductive feature is commonly ascribed to the relaxation of adsorbed intermediates involved in the anodic dissolution process [28,29]. As is frequently noted for adsorbed intermediates in acidic corrosion systems, the low-frequency inductive loop was not included in the fitting because of its weak contribution and instability.

The corresponding Bode plots (**Figures 3a-3d**) show a single, well-defined time constant, confirming that the corrosion process is governed by a single charge-transfer mechanism.

The experimental impedance data were fitted to the equivalent circuit model shown in **Figure 4.** This model represents the physical electrode-electrolyte interface, where the charge-transfer resistance (R_{ct}), the resistance between the metal and the outer Helmholtz plane that governs the corrosion rate, is connected in parallel with a CPE representing the non-ideal double layer, and both are in series with the solution resistance (R_s). The primary parameters derived from this fitting, R_{ct} and CPE, are summarized in **Table 4.**

The inhibition efficiency (IE%) and surface coverage (θ) were calculated from the charge-transfer resistance values using the following equations:

$$\theta = \left(1 - \frac{R_{ct}^{o}}{R_{ct}}\right) \quad (6)$$

$$\%IE = \left(1 - \frac{R_{ct}^{o}}{R_{ct}}\right) \times 100 \quad (7)$$

Where R^{o}_{ct} and transfer resistances for uninhibited and inhibited solutions, respectively.

Analysis of the data reveals a clear trend: the value of R_{ct} increases markedly with increasing Q-22 concentration, while the effective double-layer capacitance (C_{dl}) decreases. The increase in R_{ct} signifies a higher energy barrier for the corrosion reaction, directly leading to the observed enhancement in inhibition efficiency (up to 97% at 277 μmol L^{-1}). The concurrent decrease in C_{dl} suggests the displacement of water molecules and aggressive ions from the interface by adsorbed Q-22 inhibitor molecules, leading to either an increase in the thickness of the protective layer or a decrease in the local dielectric constant [30]. This behavior is inconsistent with the adsorption of Q-22 molecules, forming an insulating barrier that effectively shields the CS surface from the corrosive HCl medium.

The high inhibition performance is attributed to the multifunctional molecular structure of Q-22, which features a quaternary ammonium center (N^+) for strong electrostatic adsorption and a polar gluconate tail with multiple electron-donating oxygen atoms, facilitating robust surface coverage.

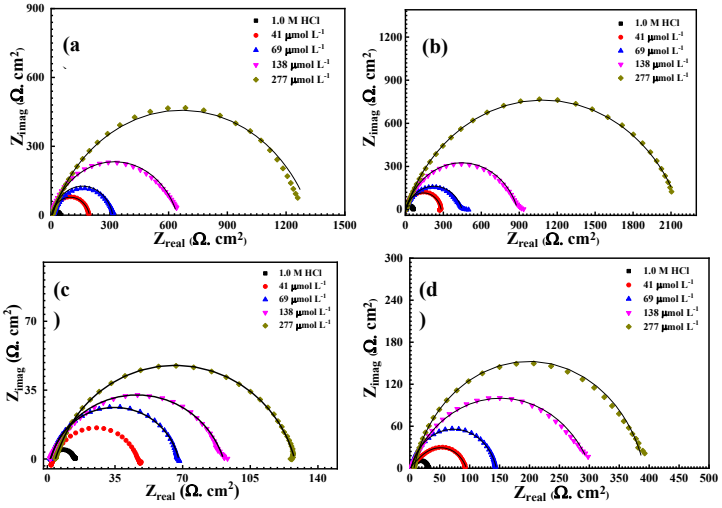

Figure 2. Nyquist plots for CS in 1.0 M HCl without and with Q-22 at (a) 20, (b) 30, (c) 40, and (d) 50 °C.

 doi:10.20944/preprints202602.1773.v1

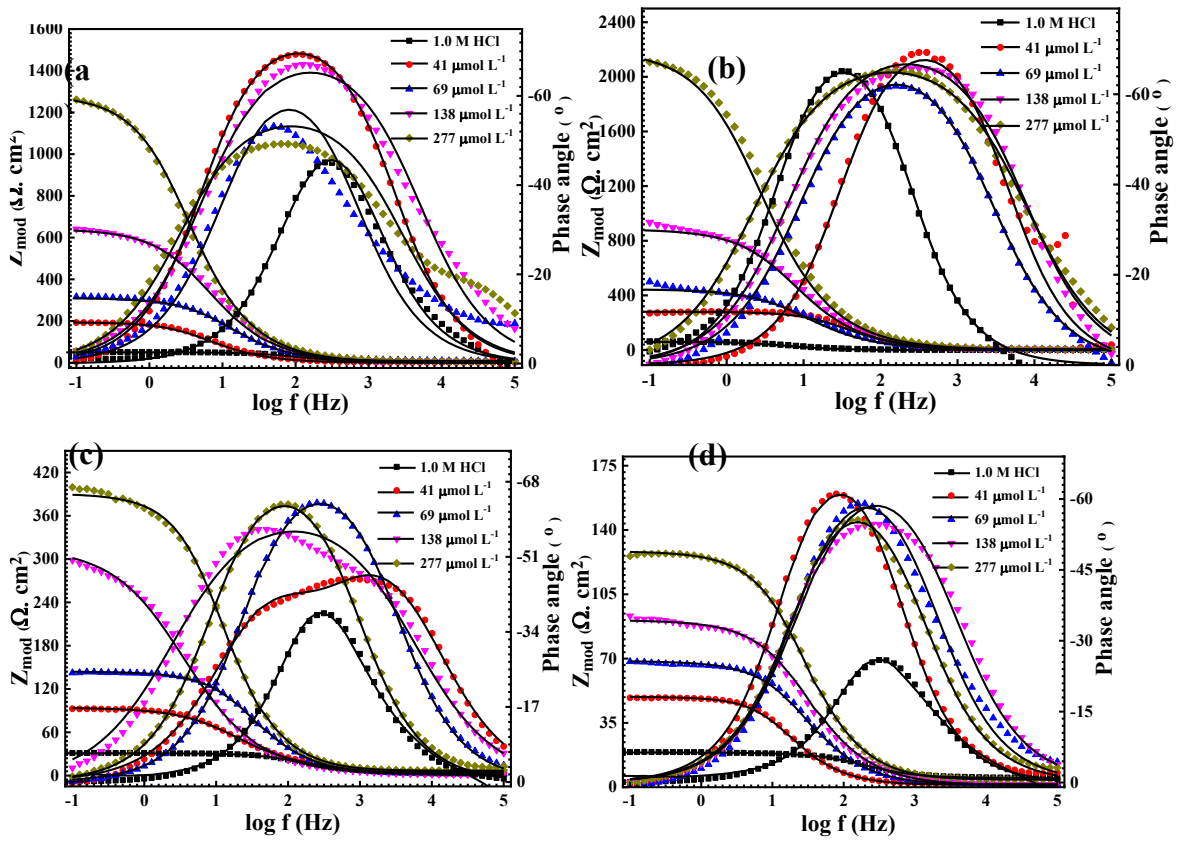

Figure 3. Bode plots (modulus and phase angle) corresponding to the conditions in Figure 2.

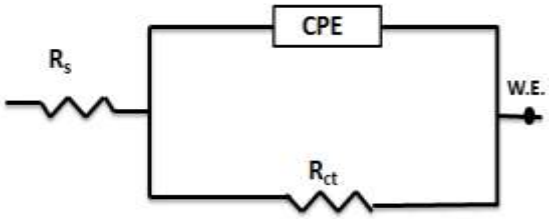

Figure 4. The exact equivalent circuit model used to fit the obtained impedance spectra.

Table 4. Fitted EIS parameters, and inhibition efficiency for CS in 1.0 M HCl solution in the absence and presence of different concentrations of Q-22 inhibitor at (a) 20, (b) 30, (c) 40, and (d) 50 °C.

T (°C)	C_{inh} (µmol L^{-1})	R_{ct} (Ω cm^2)	Y_o x 10^{-6} µΩ^{-1} s^n cm^{-2}	*Cdl, µF*	n	*θ*	*%IE*
20°	Blank	59.63	570	267.04	0.918	----	----
	41	271.5	34.8	58.65	0.884	0.781	78.14
	69	459.2	86.76	34.68	0.806	0.870	87.01
	138	934.5	56.82	17.04	0.808	0.936	93.60
	277	2104	58.41	7.57	0.770	0.971	97.00
30°	Blank	45.7	649.6	348.44	0.897	----	----
	41	192.8	257.2	82.59	0.861	0.762	76.29
	69	316.6	106.7	50.30	0.832	0.855	85.55

 doi:10.20944/preprints202602.1773.v1

	138	640.6	98.22	24.86	0.799	0.928	92.28
	277	1259	65.01	12.65	0.808	0.963	96.63
40°	Blank	30.7	709.3	518.68	0.893	----	----
	41	92.26	146	172.59	0.767	0.667	66.72
	69	142.5	102.1	111.74	0.847	0.784	78.45
	138	297.9	459.7	53.45	0.854	0.896	89.67
	277	399.6	87.64	39.85	0.702	0.923	92.23
50°	Blank	18.9	886.4	842.52	0.871	----	----
	41	48.6	181.2	327.65	0.843	0.611	61.11
	69	66.88	262.4	238.09	0.826	0.717	71.74
	138	89.61	214.5	177.70	0.800	0.789	78.90
	277	127.1	154.3	125.28	0.821	0.851	85.12

3.2.2. Potentiodynamic Polarization

Potentiodynamic polarization (PDP) curves for CS immersed in 1.0 M HCl solution, both without and with varying concentrations of the surfactant Q-22, measured at different temperatures (20, 30, 40, and 50 °C), are presented in **Figure 5 (a)– 5(d).** Key corrosion parameters derived from these curves, such as corrosion current density (i_{corr}), corrosion potential (E_{corr}), anodic and cathodic Tafel slopes (β_c and β_a), degree of surface coverage (θ), and inhibition efficiency (%IE), were all evaluated as a function of Q-22 concentration and solution ambient temperature, as summarized in **Table 5.**

The polarization resistance (R_p) was calculated using the Stern–Geary equation:

$$R_p = \frac{\beta_a \beta_c}{2.303\, i_{corr}(\beta_a + \beta_c)} \quad \textbf{(8)}$$

The inhibition efficiency (IE%) and surface coverage (θ) were determined from the corrosion current density (i_{corr}):

$$\mathrm{IE\%} = \Theta \times 100 = = \frac{\mathrm{i_{corr1}} - \mathrm{i_{corr2}}}{\mathrm{i_{corr1}}} \times 100 \quad \textbf{(9)}$$

where $\mathrm{i_{corr1}}$ and $\mathrm{i_{corr2}}$ are the corrosion current densities in the absence and presence of the inhibitor, respectively.

Analysis of the polarization curves and **Table 5** reveals several key findings:

I. The obtained cathodic and anodic polarization curves exhibit Tafel-type behavior. Addition of the investigated inhibitors to the corrosive acid medium decreases the anodic polarization current more than the cathodic one at all temperatures (mixed control) with a concomitant shift of E_{corr} towards positive values. The pronounced positive shift in E_{corr} values and the greater suppression of the anodic branch classify Q-22 as a mixed-type inhibitor with a predominant anodic effect [31,32], which preferentially restrains the anodic reaction of CS corrosion in HCl solution [33]. A shift in E_{corr} greater than 85 mV is commonly used as a benchmark to categorize inhibitors as either anodic or cathodic [34]. Therefore, despite the anodic predominance, both anodic and cathodic reactions are inhibited.

II. The corrosion current density ($i_{corr.}$) for CS in 1.0 M HCl solution decreases with increasing inhibitor concentration (Q-22), which indicates that the presence of these compounds retards the dissolution of CS in 1.0 M HCl solution, and the degree of inhibition depends on both concentration and temperature of the corrosive medium. A maximum inhibition efficiency of 97.21% was achieved at the optimal concentration of 277 μmol L^{-1}. This concentration-dependent behavior is characteristic of adsorption-based inhibitors forming a protective layer on the metal surface [35]. However, a temperature-dependent decrease in efficiency at fixed

 doi:10.20944/preprints202602.1773.v1

concentrations suggests thermal desorption of the inhibitor, compromising the protective layer [36]. The inhibition efficiencies calculated from potentiodynamic polarization align closely with gravimetric measurements.

III. The slopes of the cathodic and anodic Tafel curves (βc and βa) are slightly changed on increasing the concentration of the tested compound. This indicates that the fundamental corrosion reaction mechanism is unaltered. The fact that the values of βc are slightly higher than βa suggests that the inhibitive action of this inhibitor is by blocking the active sites on the CS surface, forming a barrier film without changing the reaction kinetics and consequently decreasing the surface area available for the electrochemical reactions [37, 38].

Table 5. Electrochemical parameters from potentiodynamic polarization for CS corrosion in 1.0 M HCl with varying Q-22 concentrations and temperatures.

T (°C)	C_{inh} µmol L^{-1}	-Ecorr (mV) SCE	i_{corr} (µA cm^{-2})	β_a, mV $decade^{-1}$	β_c, mV $decade^{-1}$	Rp, Ω cm^2	CR, mpy	θ	IE %
20	Blank	407	439	170.9	224.8	96.15	401.4	----	----
	41	409	95.1	107.6	164.1	296.73	43.47	0.781	78.14
	69	453	50.2	80.5	110.3	402.53	22.93	0.890	89.01
	138	449	29	45.6	79.3	433.49	13.24	0.936	93.62
	277	487	13.1	34.8	60.8	733.61	7.381	0.972	97.20
30	Blank	405	780	229.7	283.7	70.75	713.2	----	----
	41	441	209	77.6	110	94.53	95.41	0.732	73.29
	69	408	111	50.8	120.7	139.86	50.5	0.865	86.55
	138	409	76.1	87.8	146.1	312.92	34.78	0.902	90.28
	277	411	36.1	59.4	111.5	466.14	16.51	0.956	95.63
40	Blank	396	1187	362.8	332.5	63.54	1085	----	----
	41	427	401.0	65.3	126.7	46.66	183.4	0.667	66.72
	69	441	265	86.7	142.8	88.39	121.1	0.764	76.45
	138	433	175	99.3	97.1	121.81	80.07	0.856	85.67
	277	408	101	50	109.0	147.36	46.11	0.912	91.23
50	Blank	389	1443	371.5	361.1	55.17	1319	----	----
	41	482	600	128.9	237.6	60.48	274.3	0.581	58.11
	69	425	430	119.6	238.6	80.45	196.3	0.707	70.74
	138	426	384	124.2	220.6	89.85	175.6	0.739	73.90
	277	425	232	71.9	109.1	81.11	105.9	0.841	84.12

 doi:10.20944/preprints202602.1773.v1

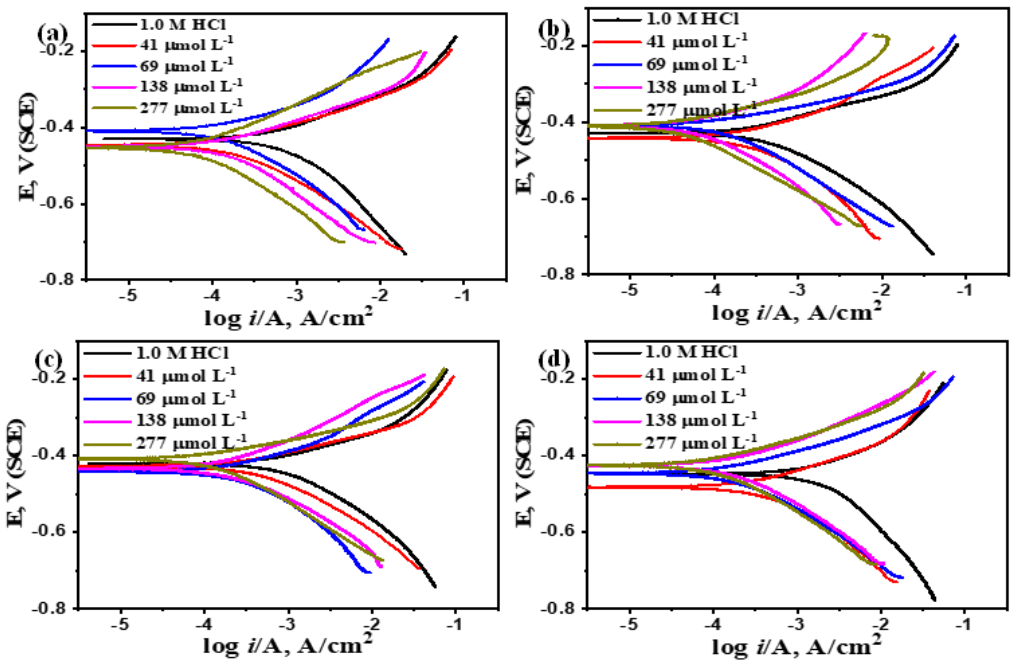

Figure 5. Potentiodynamic polarization curves for CS in 1.0 M HCl without and with Q-22 at (a) 20, (b) 30, (c) 40, and (d) 50 °C.

3.3. Adsorption Studies and Thermodynamic Isotherm

Adsorption isotherms describe the relationship between the concentration of an inhibitor in solution and the extent of its adsorption on a metal surface at constant temperature. These equations are generally expressed as [39]:

$$f(\theta,x)\exp(-a,\theta)=KC_{inh} \quad \textbf{(10)}$$

where $f(\theta, x)$ is the configurational factor depending on the physical model and assumptions of the isotherm, a is a molecular interaction constant independent of surface coverage (θ), and K is the equilibrium constant for the adsorption–desorption process. The standard free energy of adsorption ($\Delta G°_{ads.}$) is related to K_{ads} through the following expression [40]:

$$K_{ads} = 1/55.5 \exp(-\Delta G°_{ads.} / RT) \quad \textbf{(11)}$$

Here, 55.5 represents the molar concentration of water in the solution, R (8.314 J mol^{-1} K^{-1}) is the universal gas constant, and T is the absolute temperature in Kelvin.

To understand the adsorption mechanism of Q-22 molecules on the CS surface, adsorption isotherm calculations were conducted. The surface coverage (θ), calculated as θ = %IE/100 from polarization data, was used to fit the most appropriate adsorption model.

Various isotherms, Temkin, Freundlich, Frumkin, and Langmuir, were tested to determine the adsorption behavior. The experimental data showed the highest correlation coefficient (R^2) with the Langmuir isotherm, indicating monolayer adsorption of Q-22 molecules on the CS surface. The Langmuir model is expressed as:

$$C/\theta = 1/K_{ads} + C \quad \textbf{(12)}$$

where C is the equilibrium inhibitor concentration (mol L^{-1}), θ is the fractional surface coverage, and K_{ads} is the adsorption equilibrium constant (L mol^{-1}). The parameter K_{ads} reflects the strength of interaction between the inhibitor and metal surface; a higher value signifies stronger adsorption and higher inhibition efficiency.

$$\log\theta = \log K_{ads} + \frac{1}{n}\log C_{inh} \quad \textbf{(13)}$$

 doi:10.20944/preprints202602.1773.v1

While 1/n is a function of the strength of adsorption during the adsorption process, the constant K_{ads} is an estimated measure of adsorption capacity [41]. The division between the two phases is independent of concentration if n = 1. A normal adsorption is indicated if 1/n is less than one. Conversely, cooperative adsorption is indicated if 1/n is greater than one [42]. The empirical finding that the quantity adsorbed rises more slowly and that bigger concentrations are needed to saturate the surface is reflected in the constants K_{ads} and n as the temperature rises.

Figure 6 displays a Langmuir adsorption plot of C/θ vs. C_{inh} for the adsorbed organic chemical (Q-22) on the surface of CS in a 1.0 M HCl acid solution at 20, 30, 40, and 50 °C. **Figures 6 and 7** provide a linear relationship showing that the adsorption of the tested chemicals (Q-22) on the CS surface obeys Langmuir's adsorption isotherm. The slope value is equal to unity, and the intercept value is equal to $1/K_{ads}$.

Table 6 demonstrates that K_{ads} values fall as the temperature rises. This finding suggests that certain adsorbed inhibitor molecules are desorbed from the surface as a result of the temperature increase. In fact, it aligns with the suggested physisorption process [43]. The strength between the adsorbent and adsorbate is commonly indicated by K_{ads}. Higher K_{ads} values indicate more effective adsorption and, hence, more effective protection.

The standard free energy of adsorption ($\Delta G°_{ads}$) and the equilibrium constant of adsorption (K_{ads}) are connected, as may be determined using Equation (10). However, the Van't Hoff equation [44] could be used to compute the standard enthalpy of adsorption (ΔH^0_{ads}):

$$lnK_{ads} = -\frac{\Delta H^{o}_{ads}}{RT} + \frac{\Delta S^{o}_{ads}}{R} \quad \textbf{(14)}$$

or,

$$\frac{dlnK_{ads}}{dT} = \frac{\Delta H^{o}_{ads}}{RT^2}$$

A plot of ln K_{ads} versus $1/T$ (**Figure 7**) provides a linear fit, from which ΔH°_{ads} can be determined from the slope ($-\Delta H^{\circ}_{ads}$ /R). The intercept yields the entropy term (ΔS°_{ads} /R). Using these values listed in **Table 7**, the standard entropy of adsorption (ΔS°_{ads}) was calculated from the Gibbs–Helmholtz relation:

$$\Delta G^{o}_{ads} = \Delta H^{o}_{ads} - T\Delta S^{o}_{ads} \quad \textbf{(15)}$$

It is widely acknowledged that adsorption types are considered physisorption for values of ΔG°_{ads} up to −20 kJ mol^{-1}, indicating that the inhibitory effect is caused by the electrostatic interaction between charged molecules and charged metal. Chemisorption, which is caused by charge sharing or transfer from the inhibitor molecules to the metal surface to create a coordinated type of bond, is identified by values of ΔG°_{ads} around −40 kJ mol^{-1} or more negative [45]. The free energy of adsorption ΔG°_{ads} values in the current work are found to be negative, and changes for Q-22 are 37.4 to 39.8 kJ mol^{-1} required for a comprehensive adsorption. Mixed adsorption, also known as chemi/physisorption, has recently been found to have free energy change values between -28 and -38 kJ mol^{-1} [46, 47]. The results of the present study are therefore consistent with the chemi/physisorption method of adsorption [48–50]. Furthermore, the fact that %IE decreases as temperature rises indicates that physical adsorption is the primary mechanism [51].

The negative sign of ΔH°_{ads} **(Table 7)** confirms that the adsorption process is exothermic [44, 52], while the positive ΔS°_{ads} values indicate increased randomness at the metal–solution interface

 doi:10.20944/preprints202602.1773.v1

during adsorption. This entropy increase can be attributed to the displacement of water molecules from the steel surface by inhibitor molecules, leading to a more disordered interfacial region [53]. Consequently, the combined thermodynamic results affirm that Q-22 adsorption on carbon steel in 1.0 M HCl occurs spontaneously through a mixed physisorption–chemisorption mechanism, forming a stable and protective adsorbed layer.

Table 6. Parameters of the linear regression.

Temperature (K)	K_{ads} (L mol^{-1})	$(1/K_{ads}$ L mol$^{-1})$ (intercept)	R^2
293	84.3	1.88	0.999
303	74.1	1.93	0.999
313	50.4	1.95	0.999
323	41.4	2.02	0.996

Table 7. Standard thermodynamic parameters for the adsorption of Q-22 molecules on the carbon steel surface in 1.0 M HCl solution.

Temp, (K)	Langmuir isotherm		
	$\Delta G^{o}_{ads.}$ (kJ mol^{-1})	$\Delta H^{o}_{ads.}$ (kJ mol^{-1})	$\Delta S^{o}_{ads.}$ (J mol^{-1} K^{-1})
293	**-37.4**	**- 8.32**	99.3
303	**-38.5**		99.2
313	**-38.9**		97.5
323	**-39.8**		98.4

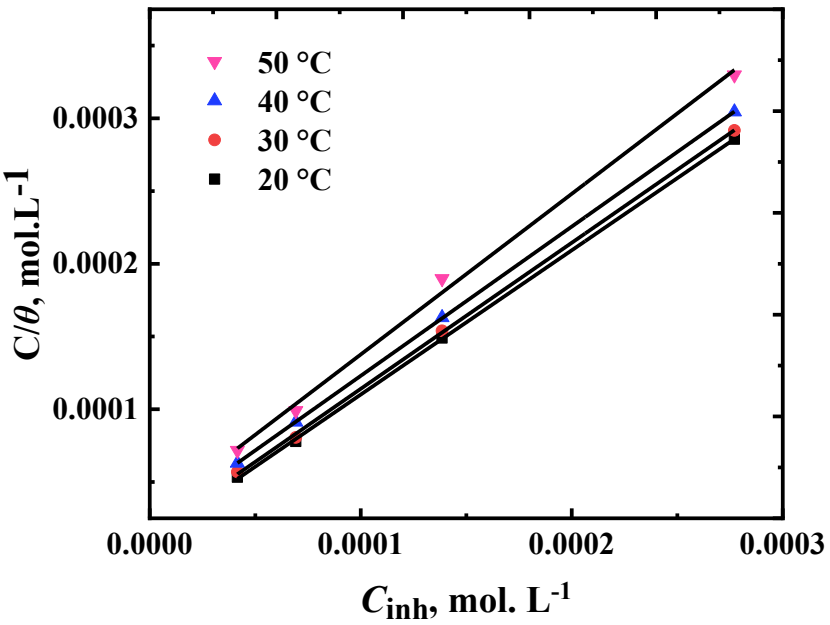

Figure 6. Langmuir adsorption isotherm for Q-22 on the CS in 1.0 M HCl at various temperatures (derived fromTafel polarization data).

 doi:10.20944/preprints202602.1773.v1

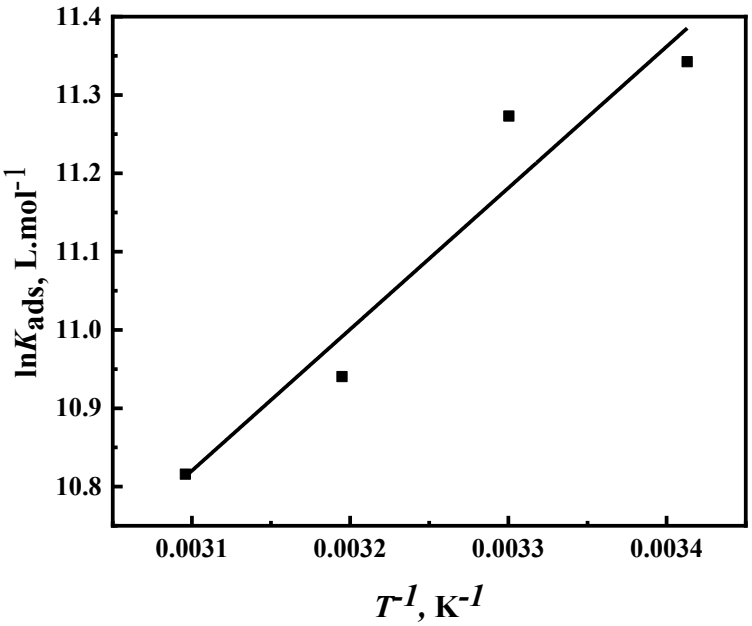

Figure 7. Van't Hoff Relationship between ln K_{ads} and 1/T for the adsorption of Q-22 molecules on CS surface in 1.0 M HCl solution.

3.4. Corrosion Kinetic and Thermodynamic Studies

To better understand the inhibition mechanism of Q-22 on CS in 1.0 M HCl, kinetic and thermodynamic analyses were carried out. These evaluations provide insight into the energy barriers and molecular interactions involved in the corrosion and inhibition processes.

The apparent activation energy (E_a), enthalpy of activation (ΔH^*), and entropy of activation (ΔS^*) for carbon steel dissolution were determined in both uninhibited and inhibited media using the Arrhenius and transition-state models [54]. The temperature dependence of the corrosion rate, expressed through the corrosion current density (i_{corr}), was fitted to the Arrhenius relationship:

$$\text{Rate} = A \exp(-\Delta E_a/RT) \quad \textbf{(16)}$$

and the transition-state equation:

$$\text{Rate} = RT/Nh \exp(\Delta S^*/R) \exp(-\Delta H^*/RT) \quad \textbf{(17)}$$

where A is the frequency factor, h is Planck's constant, N is Avogadro's number, R is the universal gas constant, and T is the absolute temperature in K.

Linear plots of log i_{corr} vs. 1/T, **Figure 8,** and log (i_{corr} /T) vs. 1/T, **Figure 9,** produced straight lines whose slopes correspond to $-E_a/2.303R$, and $-\Delta H^*/2.303R$, respectively. The intercepts of these plots yield (2.303 log A) and (log (R/Nh) + $\Delta S^*/2.303R$) for Arrhenius and transition-state equations. The resulting activation parameters (the apparent activation energy, E_a, activation entropies, ΔS^*, and activation enthalpies, ΔH^*) are summarized in **Table 8**. The values of activation energy (E_a) were consistently higher in the presence of surfactant Q-22 than in its absence, and E_a increased with inhibitor concentration. This trend indicates that the surfactant molecules create an energetic barrier by adsorbing onto the steel surface and blocking active corrosion sites, thereby impeding charge-transfer reactions [55].

The activation parameters ΔH* and ΔS* were further evaluated using the transition-state formulation, an alternative form of the Arrhenius equation [56].

$$CR = \frac{RT}{Nh} exp^{\frac{\Delta S^*}{R}} \exp^{\frac{-\Delta H^*}{RT}} \quad \textbf{(18)}$$

 doi:10.20944/preprints202602.1773.v1

In this expression, the corrosion rate (*CR*) depends on *N* (Avogadro's number), *R* (the universal gas constant), *h* (Planck's constant), and *T* (temperature in Kelvin). The parameters ΔH* and ΔS* represent the enthalpy and entropy of activation, respectively.

All systems exhibited positive ΔH* values, confirming that the corrosion of carbon steel in HCl is an endothermic process. Moreover, both ΔH* and ΔS* values were lower than the corresponding E_a, suggesting that the transition from reactants to the activated complex requires energy input and involves a more ordered configuration. Notably, the relatively high and negative values of ΔS* suggest that the transition from reactants to the activated complex involves a decrease in system randomness. This behavior implies that during the rate-determining step, the transition complex is more ordered, representing an association rather than a dissociation process [57,58].

The magnitude and sign of ΔS* further suggest that the corrosion process, especially in the presence of Q-22, involves the formation of a structured interface where inhibitor and water molecules organize around the carbon steel surface. Such ordering facilitates the adsorption of Q-22 molecules onto the metal surface, stabilizing the protective layer and minimizing the availability of active corrosion sites.

Moreover, as the concentration of Q-22 increases, both Ea and ΔH* rise, signifying that the inhibitor elevates the energy threshold required for corrosion reactions to occur. Concurrently, the increasingly negative ΔS* values indicate a greater degree of surface organization, corresponding to the development of a compact, adsorbed inhibitor film that effectively hinders both the anodic and cathodic processes.

Overall, the kinetic and thermodynamic analyses confirm that Q-22 acts as an efficient corrosion inhibitor for CS in 1.0 M HCl. It suppresses metal dissolution primarily through adsorption, forming a dense, thermally stable film that reduces reaction kinetics and alters the energetic landscape to favor surface passivation.

Table 8. Activation Energy (Ea), Enthalpy of activation (ΔH*), and Entropy of activation (ΔS*) for CS in 1.0 M HCl solution in the absence and presence of different concentrations of the Q-22 corrosion inhibitor.

C_{inh} (μmol L^{-1})	E_a (kJ mol^{-1})	ΔH^* (kJ Mol^{-1})	ΔS^* (J mol^{-1} K^{-1})
0	31.5	29.01	-209.354
41	48.8	46.23	-163.387
69	57.6	55.12	-138.662
138	67.6	65.05	-109.429
277	76.01	73.46	-87.493

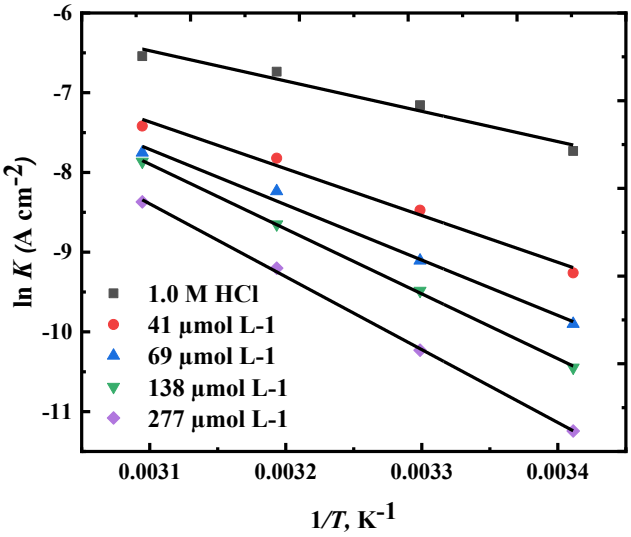

 doi:10.20944/preprints202602.1773.v1

Figure 8. Arrhenius relationship between log i_{corr} and 1/T for CS in 1.0 M HCl, obtained at various concentrations of the Q-22 corrosion inhibitor.

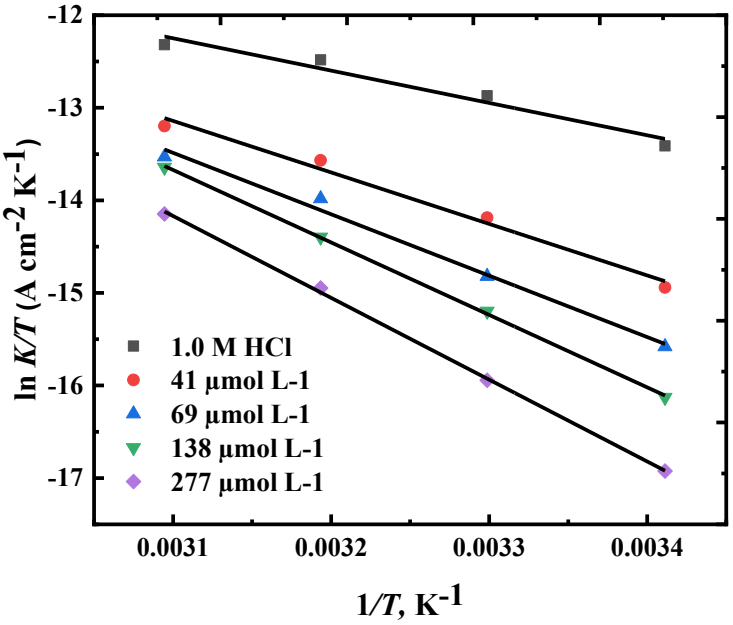

Figure 9. Transition-state plots of log (i_{corr}/T) versus 1/T for CS immersed in 1.0 M HCl solution, illustrating the effect of different Q-22 inhibitor concentrations on the activation parameters of the corrosion process.

3.5. Surface Characterization

3.5.1. Scanning Electron Microscopy (SEM) Analysis

The surface morphology of CS was examined using scanning electron microscopy (SEM) to provide direct visual evidence of corrosion and inhibition. Samples were analyzed in three states: pristine (unexposed), after 24 h immersion in uninhibited 1.0 M HCl, and after immersion in HCl containing 277 µmol L^{-1} Q-22. Scanning Electron Microscopy (SEM) works by directing a focused beam of electrons over the surface of a sample. The interaction between the electrons and the atoms of the sample generates signals from secondary and backscattered electrons. These signals are then collected to create high-resolution images that offer detailed insights into the surface topography, microstructural changes, and the presence of corrosion products or protective films [59, 60].

The SEM micrographs are presented in **Figure 10 (a, b),** which depict scanning electron micrographs of an unexposed specimen of CS, alongside a CS sample that was exposed 24 hours to a blank 1.0 M HCl solution. **Figure 10 (c)** displays scanning electron micrographs of CS specimens that were exposed for 24 hours to a 1.0 M HCl solution containing 277 µmol L^{-1} of Q-22.

Figure 10 (a) illustrates that the surface of the pristine carbon steel (CS) metal is entirely free from any pits or cracks. In contrast, **Figure 10 (b)** shows significant damage across the entire CS surface after being immersed in a 1.0 M HCl solution, characterized by uniform corrosion and extensive surface roughness and etching. **Figure 10 (c)** indicates that, in the presence of 277 µmol L^{-1} of the Q-22 inhibitor, the metal surface is largely covered by an adsorbed inhibitor layer. This treatment results in much less corrosion compared to the specimen exposed to the acid solution without the inhibitor, effectively reducing the formation of corrosion pits and impeding direct acid attack on the steel substrate.

Better results can be seen from the micrograph with the presence of 277 µmol L^{-1} Q-22 depicted in **Figure 10 (c).** Thus, examining micrographs reveals that the inhibitor molecules Q-22 give higher

 doi:10.20944/preprints202602.1773.v1

adsorption on the surface, resulting in the formation of a protective inhibition film, which supports the chemical and electrochemical results well. Additionally, these microstructural features confirm that Q-22 molecules adsorb strongly on the CS surface, forming a stable, adherent, and continuous barrier film.

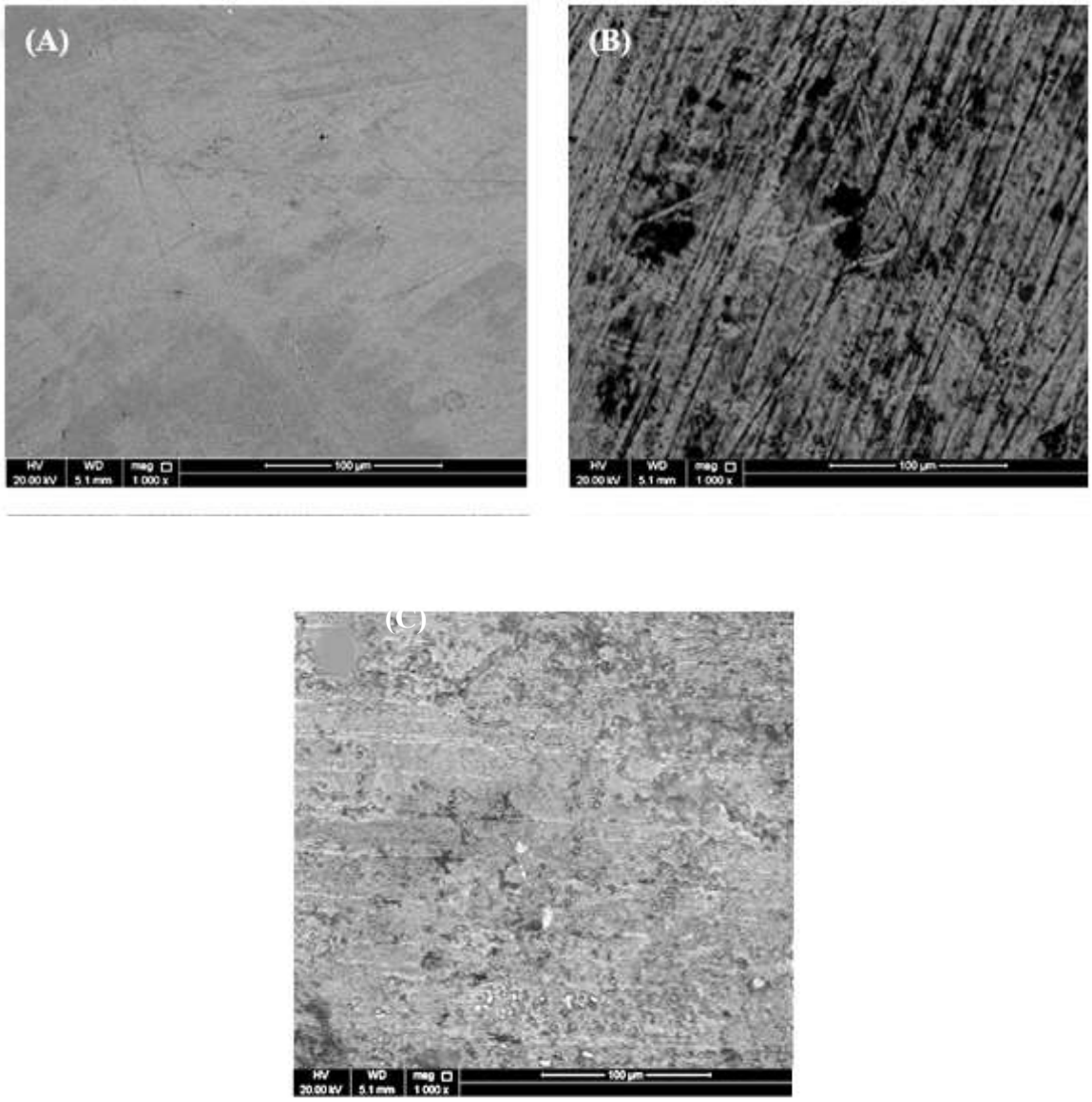

Figure 10. Scanning electron micrographs of CS surfaces: **(A)** polished (reference state), **(B)** after 24 h immersion in 1.0 M HCl at 20 °C (blank), and **(C)** after 24 h immersion in 1.0 M HCl containing 277 μmol L^{-1} Q-22 at 20 °C.

3.5.2. AFM Analysis

Atomic Force Microscopy (AFM) was utilized to quantitatively assess the surface topography and roughness of CS samples after 24 hours of immersion at 20 °C, both in uninhibited and Q-22-inhibited (277 μmol L^{-1}) HCl. AFM provides three-dimensional surface images and nanoscale roughness measurements, offering valuable insight into the microstructural effects of corrosion and the protective film formation induced by inhibitors [59, 61].

The root mean square (RMS) roughness was used as a key parameter to evaluate the extent of surface degradation and the effectiveness of the inhibitor. The RMS value reflects the degree of surface irregularity: a higher RMS corresponds to more severe corrosion, while a lower RMS indicates

 doi:10.20944/preprints202602.1773.v1

a smoother and more protected surface. The measured RMS values for the different samples are summarized in **Table 9**, and representative AFM micrographs are presented in **Figures 11(a–c).**

Figure 11 (a) displays the three-dimensional surface topography of a blank CS specimen, whereas **Figure 11 (b)** presents the atomic force micrograph of a CS specimen after immersion in 1.0 M HCl solution. **Figure 11 (c)** shows the atomic force micrographs of a CS specimen in 1.0 M HCl solution containing (277 µmol L-1 Q-22) corrosion inhibitor, all after 24 h immersion at 20 °C.

The surface morphology of the CS was severely corroded when exposed to an HCl solution without an inhibitor. This can be qualitatively seen from AFM micrographs, as there is the formation of deep holes and pits due to the aggressive chloride environment, giving a high RMS value of approximately 200 nm.

The average RMS value for CS is significantly reduced to 30 nm in the presence of (277 µmol L^{-1} Q-22). The smoothness and homogeneity of the surface are due to the formation of a compact protective film on the metal surface, which can effectively inhibit the corrosion of CS in HCl solution.

The above parameters observed for CS in the presence of (277 µmol L-1 Q-22) corrosion inhibitor is smaller than the AFM data of polished metal surface in hydrochloric acid, which confirms the formation of an adsorbed film on the surface having the ability to protect and isolate the metallic substrate from the aggressive environment. This organic layer acts as a physical barrier, impeding the diffusion of corrosive ions and preventing localized acid attack on the substrate [62, 63].

These results confirm that Q-22 molecules adsorb onto the CS surface to form a compact and highly protective film. The significant reduction in RMS roughness from 200 nm to 30 nm provides direct, quantitative proof of the film's efficacy in preventing corrosion.

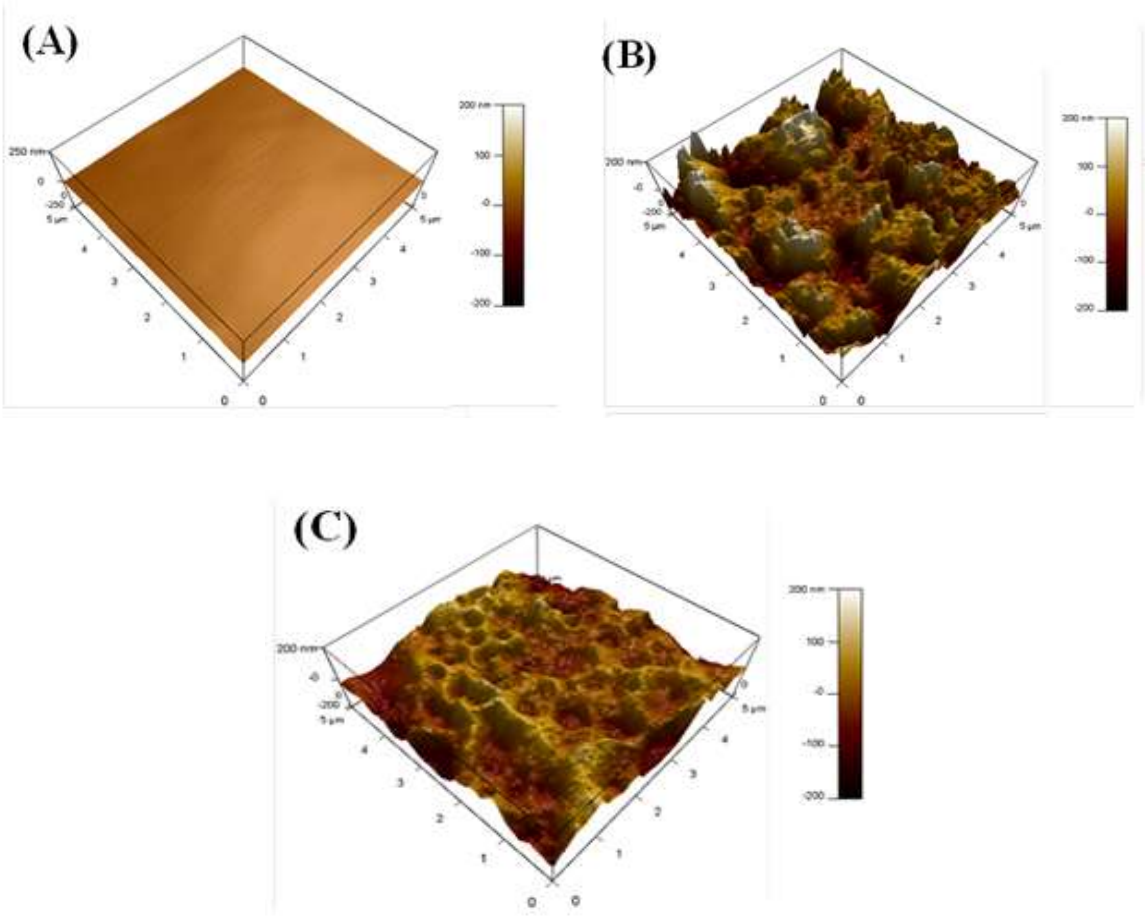

 doi:10.20944/preprints202602.1773.v1

Figure 11. Atomic force microscopy (AFM) analysis of CS surfaces after 24 h at 20 °C (A) polished blank, (B) after immersed in 1.0 M HCl solution, and (C) after immersed in 1.0 M HCl solution + 277 µmol L-1 Q-22, all after 24 h immersion at 20 °C.

Table 9. Surface roughness parameters derived from atomic force microscopy (AFM) analysis of carbon steel samples after 24 h immersion at 20 °C under different conditions.

No.	CS sample	Roughness (Ra)/nm
A	Blank (Polished CS)	10
B	1.0 M HCl (Corroded CS)	200
C	1.0 M HCl + 277 µmol L^{-1} Q-22 (Inhibited CS)	30

3.5.3. XPS Analysis

High-resolution X-ray photoelectron spectroscopy (XPS) was employed to elucidate the chemical composition and bonding characteristics of the protective film developed on the CS surface after immersion in 1.0 M HCl containing the Q-22 inhibitor. The survey spectra revealed the presence of characteristic peaks corresponding to Fe 2p, O1s, C1s, and N1s, confirming the coexistence of metallic and organic constituents on the surface.

Figure 12 illustrates the XPS survey spectra of CS specimens immersed for 24 hours in 1.0 M HCl, both in the absence and presence of 277 µmol L^{-1} Q-22. The C 1s spectrum (**Figure 13a**) of the Q-22–treated surface exhibits a dominant photoemission peak centered around 284.8 eV, which corresponds to C–C/C–H bonds typically associated with the long alkyl chains of quaternary ammonium surfactants. Additionally, a noticeable secondary peak appearing at approximately 286–287 eV is assigned to C–N bonding, confirming the incorporation of nitrogen-containing groups on the steel surface.

These observations demonstrate that the organic film detected on the surface originates from the adsorption of Q-22 molecules, verifying the formation of an inhibitor-derived protective layer rather than contamination from adventitious carbon species [63].

The **N** 1s region **Figure 13 (b)** provides further insight into the adsorption mechanism. The Q-22 spectrum exhibits multiple components: a strong quaternary $\mathbf{N^+}$ peak near **~400 eV**, together with a lower-binding-energy feature at **~398–399 eV** assigned to **Fe–N coordination**, indicating nitrogen–metal interaction [64]. The presence and relative intensity of this low-BE N component suggest that, in addition to electrostatic adsorption via its positively charged headgroup, Q-22 undergoes chemisorptive bonding with the carbon-steel surface through partial electron donation from nitrogen (and possibly oxygen) atoms to vacant Fe d-orbitals. Similar Fe–N bonding behavior has been widely observed in studies of quaternary ammonium and nitrogen-based inhibitors [65] [62] [66].

This interpretation is further corroborated by the Fe 2p spectra presented in **Figure 13(c)**, which reveals a significant reduction in the intensity of metallic iron peaks for the inhibited sample compared to the blank surface. The Fe $2p_{3/2}$ and Fe $2p_{1/2}$ components exhibit both diminished intensity and slight positive shifts in binding energy, indicating the formation of a Q-22–metal interfacial complex. These spectral changes suggest that the inhibitor molecules strongly interact with surface Fe atoms, modifying their electronic environment. The marked suppression of the Fe^0 signal, together with the reduced contribution of iron oxide species, implies the development of a compact organic protective layer that effectively isolates the metal substrate from the aggressive acidic medium. This observation confirms that Q-22 promotes efficient surface passivation through the formation of a stable and adherent film [65, 67].

Overall, the XPS results confirm that Q-22 adsorbs onto the carbon-steel surface via a mixed physical-chemical mechanism. The quaternary ammonium headgroup anchors electrostatically to the negatively charged, chloride-covered surface, while the nitrogen atoms form coordinate (Fe–N) bonds, enhancing the film's stability. Simultaneously, the long hydrophobic alkyl chains align outward, generating a compact, low-permeability barrier against acid attack. This dual mechanism—

 doi:10.20944/preprints202602.1773.v1

electrostatic attraction followed by chemisorptive stabilization—results in a strongly bound, uniform, and corrosion-resistant film [62, 61].

These XPS surface-chemical insights are fully consistent with the electrochemical and weight-loss measurements. The formation of a thicker and more cohesive film of Q-22 enhances the charge-transfer resistance (R_{ct}) observed in EIS, increases the polarization resistance (R_p), reduces the corrosion current density (i_{corr}) in Tafel polarization, and lowers the measured mass loss, collectively confirming the inhibitor's superior performance. Furthermore, analysis of the adsorption behavior using the Langmuir isotherm shows that Q-22 has a high adsorption equilibrium constant (K_{ads}) and a more negative $\Delta G°_{ads}$, indicating strong and spontaneous adsorption, which aligns with the chemisorption characteristics inferred from the N 1s spectrum [59, 65].

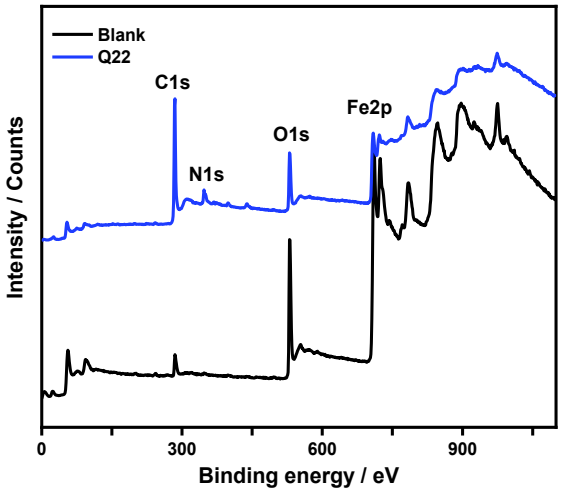

Figure 12. XPS survey spectra of the CS surface after 24 h immersion in 1.0 M HCl: (i) uninhibited (blank) and (ii) inhibited with 277 μmol L^{-1} Q-22.

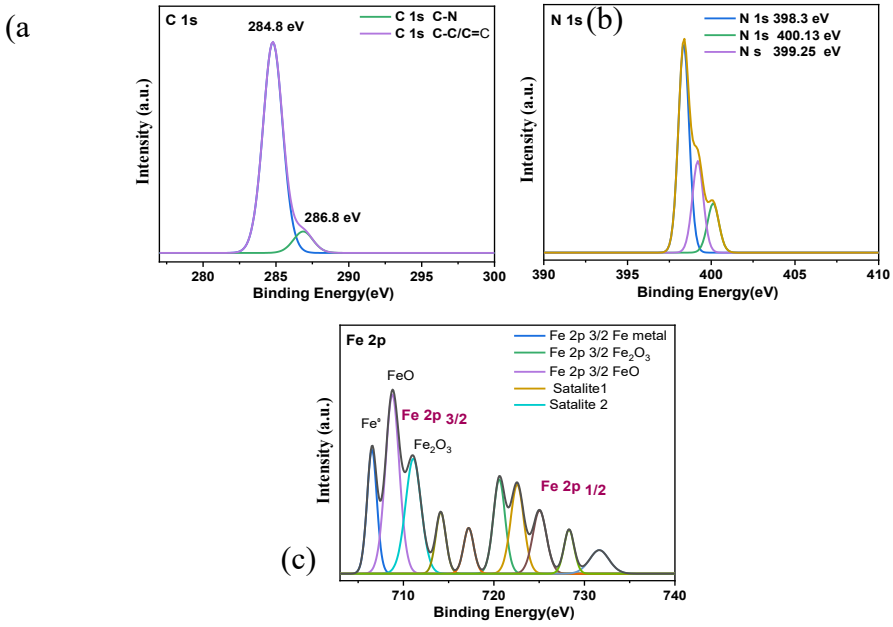

Figure 13. High-resolution XPS core-level spectra for the CS surface after 24 h immersion in 1.0 M HCl containing 277 μmol L^{-1} Q-22: (a) C 1s, (b) N 1s, and (c) Fe 2p.

 doi:10.20944/preprints202602.1773.v1

3.5.4. Surface Wettability Analysis (Contact Angle)

The protective film formed by Q-22 was further evaluated by investigating its effect on the CS surface's wettability via contact angle measurements. The wettability of a surface is a key factor in corrosion resistance, as a hydrophobic surface can act as an effective barrier against an aqueous corrosive medium by impeding electrolyte contact [68].

Figure 14 (a) shows the water contact angle for a freshly polished CS sample, which was ~63°, indicating a moderately hydrophilic surface. After immersion in the aggressive 1.0 M HCl solution without an inhibitor, the surface became highly hydrophilic, with the contact angle drastically decreasing to ~34° **Figure 14 (b).** This behavior is attributed to surface roughening and the formation of corrosion products, which increase the surface's affinity for water and facilitate wetting.

In stark contrast, the surface inhibited with 277 μmol L^{-1} of Q-22 exhibited a strongly hydrophobic character, with a contact angle of ~101° **Figure 14 (c).** This remarkable increase provides direct, quantitative evidence that Q-22 molecules form a coherent and hydrophobic film on the steel surface [69, 70]. Effective surface hydrophobization is confirmed by this value of ~101°, which is comparable to or exceeds those reported for effective hydrophobic inhibitor coatings on carbon steel (typically in the range of ~85–100°). The adsorption of Q-22, with its long alkyl chain, displaces water molecules and creates a non-polar barrier. This hydrophobic layer physically impedes the contact and penetration of the aqueous corrosive electrolyte, thereby significantly enhancing the corrosion inhibition efficiency [71]. Additionally, similar contact angle values have been documented for steel surfaces protected by effective organic inhibitors and surfactants in acidic environments [70], suggesting the development of a compact and water-repellent protective coating [72]. This result is consistent with the protective film observed in the SEM and AFM micrographs, providing a functional property (hydrophobicity) that directly explains the superior electrochemical performance of Q-22.

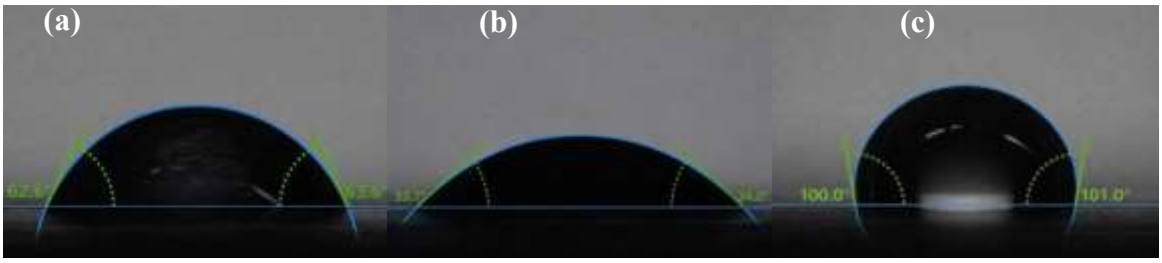

Figure 14. a), (b), and (c) showing water droplets on the polished, corroded, and inhibited surfaces, respectively, with the contact angle values clearly displayed.

3.6. DFT studies

Density Functional Theory (DFT) was employed to investigate the electronic reactivity and inhibition performance of Q-22 and its protonated form ($Q\text{-}22H^+$). Quantum chemical descriptors, including EHOMO, ELUMO, energy gap (ΔE), dipole moment (μ), ionization potential (I), electron affinity (A), electronegativity (χ), hardness (η), softness (S), electrophilicity (ω), nucleophilicity (ε), electro-accepting (ω^+) and electro-donating (ω^-) powers, back-donation energy (ΔE_back), fraction of electron transfer (ΔN), and inhibitor–metal interaction energy, were calculated and summarized in Tables 10–11. The HOMO is primarily localized on ring groups and heteroatoms, identifying these as preferred electron-donating sites, which is consistent with the improved inhibition efficiency and experimental results [73,74–77]. Smaller ΔE values, low μ, and low χ indicate high chemical reactivity, while high softness suggests effective electron donation to the carbon steel (CS) surface. Protonation increases softness and surface adherence of $Q\text{-}22H^+$, enhancing protection compared to neutral Q-22 [82,83].

Local reactivity was evaluated using Fukui functions (Eqs. 19–21) [24,25], with nucleophilic (f^+) and electrophilic (f^-) attack sites identified in Tables 12 and 11.

 doi:10.20944/preprints202602.1773.v1

$$f^{+}{}_{k} = q_k\,(N+1) - q_k\,(N) \quad (\text{nucleophilic attack}) \tag{19}$$

$$f^{-}{}_{k} = q_k\,(N) - q_k\,(N-1) \quad (\text{electrophilic attack}) \tag{20}$$

$$\Delta f_k = f^{+}{}_{k} - f^{-}{}_{k} \tag{21}$$

where $q_k(N)$,$q_k(N+1)$, and $q_k(N-1)$ are the charge values of atoms k for neutral, anionic, and cationic, respectively. Δfk is the dual descriptor that Morell et al. presented, which is calculated as the difference between the nucleophilic and electrophilic Fukui functions [85,84].

In neutral Q-22, O15, C41, and C45 are nucleophilic centers, whereas O17, O18, C19, O22, O23, and C41 are electrophilic sites. Protonation alters the active sites, creating O15 and Cl1 as nucleophilic and C49–C51 as electrophilic centers in Q-22H⁺. Molecular electrostatic potential (MEP) and electrostatic potential (ESP) maps (Figure 17) confirm that regions around heteroatoms (N, Cl, O) are electron-rich (red/yellow, nucleophilic), whereas the aromatic rings are electron-deficient (blue, electrophilic), supporting the proposed adsorption mechanism on the CS surface [86, 87].

Table 10. Computed quantum chemical descriptors for the studied neutral Q-22 and protonated Q-22 H⁺ inhibitor in the gas phase.

Descriptors	Equations	Q-22	Q-22 H⁺
Energy of highest occupied molecular orbital (E_{HOMO}), (eV)		-6.465	-6.370
Energy of lowest unoccupied molecular orbital (E_{LUMO}), (eV)		-1.052	-0.8587
Energy Gap ΔE	(LUMO-HOMO)	5.413	5.511
Dipole moment, (μ), (Debye)		16.401	17.146
Ionization energy (I) (ev)	$I = -E_{HOMO}$	6.465	6.370
Electron affinity (Y) (ev)	$Y = -E_{LUMO}$	1.052	0.8587
Electronegativity (ϕ)	$\phi = \frac{I+Y}{2}$	3.758	3.614
Global hardness ψ	$\psi = \frac{I-Y}{2}$	2.706	2.756
Global softness (S)	$s = \frac{1}{\psi}$	0.370	0.363
Global electrophilicity (ω)	$\omega = \phi^2/2\psi$	2.609	2.370
Global nucleophilicity (ε)	$\varepsilon = \frac{1}{\omega}$	0.383	0.422
Electroaccepting (ω+) power	$\omega^{+} = \frac{(I+3A)^2}{16(I-A)}$	1.068	0.9076
Electrodonating (ω⁻) power	$\omega^{-} = \frac{(A+3I)^2}{16(I-A)}$	4.827	4.522
Net electrophilicity (Δω± = ω+ +ω−)	(Δω± = ω+ +ω−)	5.895	5.430
Fraction of transferred electrons (ΔN)	$\Delta N = \frac{\phi_{Fe} - \phi_{inh}}{2(\psi_{Fe} + \psi_{inh})}$	-0.1009	-0.1197
Back-donation energy ΔE back-donation (ev)	$\Delta E_{back-donation} = -\frac{\psi}{4}$	-0.6765	-0.6890
Metal/inhibitor interaction energy $\Delta E_{Metal/inhibitor}$ (ev)	$\Delta E_{\text{Fe}\cdots\text{inh}} = \frac{(\chi_{Fe} - \chi_{inh})^2}{4(\eta_{Fe} + \eta_{inh})}$	0.0357	0.0509

 doi:10.20944/preprints202602.1773.v1

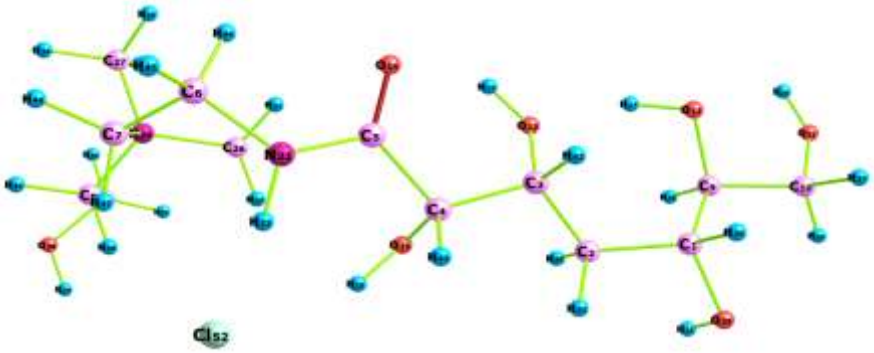

Q-22

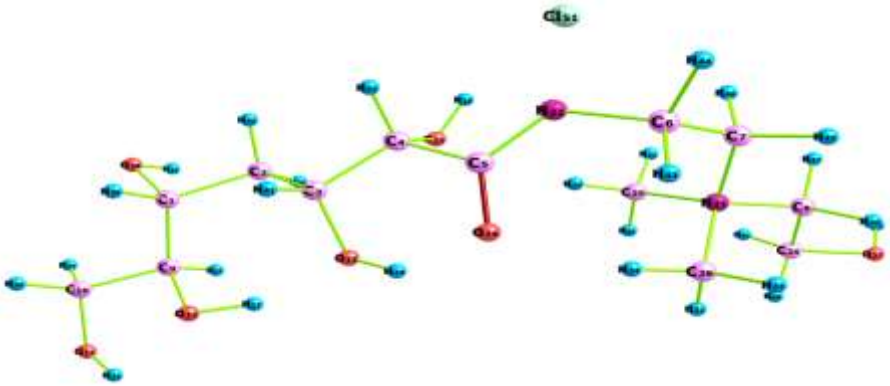

Q-22H+

Figure 15. Optimized structure of the Q-22 and Q-22H+ using the B3LYP/6-311++G(d,p) basis set.

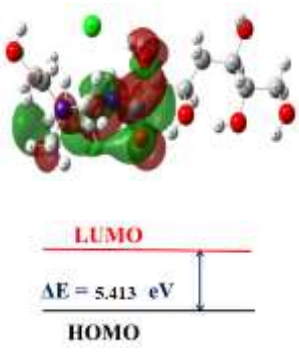

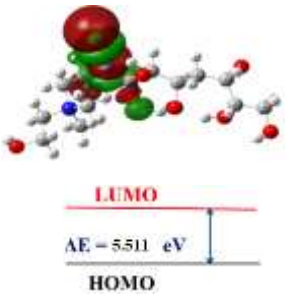

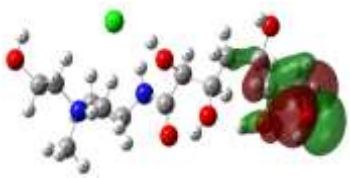

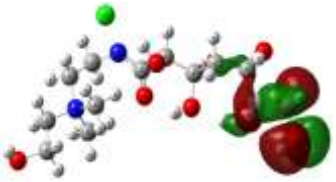

 doi:10.20944/preprints202602.1773.v1

Figure 16. Frontier molecular orbitals HOMO and LUMO of the Q-22 and Q-22H+ using the B3LYP/6-311++G(d,p) basis set.

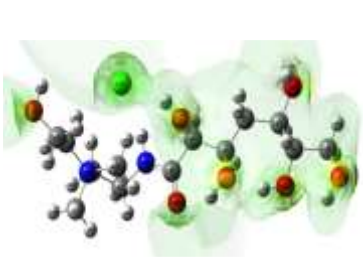

MEPofQ-22

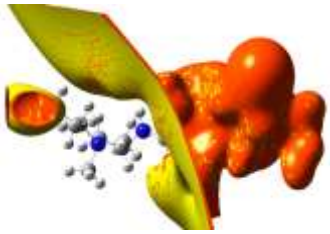

ESP of Q-22

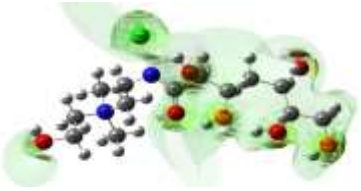

MEPofQ-22H+

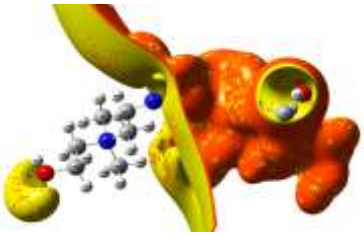

ESP of Q-22H+

Figure 17. ESP and MEP distribution of the neutral Q-22 and Q-22H+ using the B3LYP/6-311++G(d,p) basis set.

Table 11. Fukui indices of the studied Q-22 and Q-22 H+.

Q-22				Q-22H+			
Atoms	f_k^+	f_k^-	Δf_k	**atoms**	f_k^+	f_k^-	Δf_k
Cl (1)	0.022	0.003	0.019	Cl (1)	0.01	0.002	0.008
O (2)	0.028	0.001	0.027	O (2)	0.024	0.016	0.008
N (4)	0.003	0.008	-0.005	N (4)	0	0.001	-0.001
C (5)	0.014	0.005	0.009	C (5)	0.016	0.01	0.006
C (6)	0.015	0.001	0.014	C (6)	0.014	-0.001	0.015
C (7)	0.01	-0.01	0.02	C (7)	0.004	0.007	-0.003
N (9)	0.015	-0.002	0.017	N (9)	0.004	0	0.004
C (10)	0.024	-0.001	0.025	C (10)	0.023	0.008	0.015
C (11)	0.012	0.004	0.008	C (11)	0.004	0.006	-0.002
C (13)	0.021	0.003	0.018	C (13)	0.019	0	0.019
O (14)	0.01	0.015	-0.005	O (14)	0.014	0.004	0.01
O (15)	0.032	-0.002	0.034	O (15)	0.033	0.003	0.03
C (16)	-0.002	0.011	-0.013	C (16)	-0.004	-0.004	0
O (17)	-0.002	0.089	-0.091	O (17)	-0.001	-0.002	0.001
O (18)	-0.003	0.065	-0.068	O (18)	0.007	-0.009	0.016
C (19)	0.005	0.041	-0.036	C (19)	0.014	0	0.014
O (22)	0.001	0.061	-0.06	O (22)	0.01	0.005	0.005
O (23)	0.005	0.038	-0.033	O (23)	0.009	0.005	0.004
C (27)	0.001	0.004	-0.003	C (27)	-0.007	-0.004	-0.003

 doi:10.20944/preprints202602.1773.v1

Q-22				Q-22H+			
Atoms	f_k^+	f_k^-	Δf_k	atoms	f_k^+	f_k^-	Δf_k
C (28)	0.001	0.005	-0.004	C (28)	0	0	0
C (34)	-0.001	0.01	-0.011	C (34)	-0.007	-0.002	-0.005
C (35)	0.002	0.028	-0.026	C (35)	0	-0.002	0.002
C (36)	0.001	0.022	-0.021	C (36)	0.004	-0.001	0.005
C (38)	0.019	0.009	0.01	C (38)	0.013	0.001	0.012
C (39)	0.01	-0.001	0.011	C (39)	-0.003	0.023	-0.026
C (40)	0.019	0.001	0.018	C (40)	0.004	0.014	-0.01
C (41)	0.022	0.002	0.02	C (41)	0.005	0.012	-0.007
C (42)	0.019	0	0.019	C (42)	0.003	0.013	-0.01
C (43)	0.022	0.003	0.019	C (43)	0.003	0.013	-0.01
C (45)	0.037	0.005	0.032	C (45)	0.012	0.027	-0.015
C (46)	0.003	-0.003	0.006	C (46)	-0.004	0.029	-0.033
C (47)	0.006	0.004	0.002	C (47)	0.004	0.014	-0.01
C (48)	0.01	-0.001	0.011	C (48)	0.003	0.016	-0.013
C (49)	0.009	0.008	0.001	C (49)	0.002	0.015	-0.013
C (50)	0.012	0.004	0.008	C (50)	0.003	0.015	-0.012
C (51)	0.018	0.01	0.008	C (51)	0.008	0.032	-0.024

3.6.1. Natural Bond Orbital (NBO) Analysis

Natural Bond Orbital (NBO) analysis was performed to investigate charge transfer and electronic stabilization in Q-22. Second-order perturbation energies (E^2) quantify electron delocalization from filled orbitals, including bonding (BD) and lone pairs (LP), to empty antibonding (BD*) or Rydberg (RY*) orbitals, providing insight into hyperconjugation, resonance, and non-covalent interactions that stabilize the molecule [**88–91**]. The most significant contributions (**Table 12**) arise from LP(1) N24 → *πN22–C16 (65.21 kcal·mol⁻¹), LP(1) O14* → πC10–O24 (60.05 kcal·mol⁻¹), LP(1) O12 → *πC13–O26 (59.83 kcal·mol⁻¹), and πC25–O28* → πC27–O13 (55.05 kcal·mol⁻¹), with additional stabilization from N24 → πCl51–N22 (13.19 kcal·mol⁻¹). These results highlight the key role of nitrogen, oxygen, and chlorine lone pairs in hyper conjugation and electron delocalization, supporting strong inhibitor–metal interactions. Overall, the high E^2 values indicate substantial electronic stabilization of Q-22, consistent with its observed corrosion inhibition efficiency and experimental PDP, EIS, and surface analysis results.

Table 12. Second-order perturbation theory analysis of Fock Matrix in NBO Basis of Q-22 compound at B3LYP/6-311++G (d, p) level in the gas phase.

Compound	Donor	Acceptor	$E^{(2)a}$(kcal/mol)	Occupancy
Q-22	πC3–O13	π*C25–O11	23.52	1.77
	πC4–O15	π*C26–O12	25.13	1.65
	πC5–O14	π*C5–O14	33.52	1.67
	πC10–O11	π*C4–O15	35.13	1.66
	πC9–O12	π*C9–O20	44.52	1.68
	πC1–O20	π*C1–O28	36.13	1.75
	πC25–O28	π*C27–O13	55.05	1.55
	LP (1) N22	π*Cl51–N24	26.74	1.87
	LP (1) N24	π*C16–N22	65.21	1.45
	πC6–N22	π*C24–N24	36.58	1.82
	πC26–N24	π*O14–C6	16.47	1.94
	LP (1) O11	π*O23–O15	31.04	1.84
	LP (1) O12	π*C13–O26	59.83	1.75
	LP (1) O13	π*C32–O15	18.81	1.88

 doi:10.20944/preprints202602.1773.v1

	LP (1) O14	π*C10–O24	60.05	1.70
	LP (1) O15	π*O14–N22	26.74	1.57
	LP (3) Cl51	π*Cl51–H50	45.21	1.35
	LP (2) O20	π*C10–C7	36.58	1.82
	LP (2) O28	π*O15–C6	26.47	1.94

3.6.2. Molecular Simulation Dynamics

The adsorption of Q-22 on the carbon steel (CS) surface was investigated using molecular dynamics (MD) simulations. The inhibitor was positioned on a solvent-free Fe (111) surface, and the interaction (E_interaction) and binding (E_binding) energies were calculated using Eqs. (22–23) [90], yielding −732.67 kcal·mol^{-1} for both energies, indicating strong adsorption.

$$E_{interaction}=E_{total}-(E_{surface+solution}-E_{inhibitor}) \quad \textbf{(22)}$$

$$E_{binding}=-E_{interaction} \quad \textbf{(23)}$$

As shown in Figure 18, Q-22 adopts a nearly parallel orientation on the Fe surface, maximizing coverage through interactions involving aromatic π-electrons, nitrogen, oxygen, and chlorine atoms. Equilibrium parameters for Q-22 and Q-22H$^+$ are listed in Table 13, while adsorption energies are depicted in Figure 19. Radial distribution function (RDF) analysis (Figure 20) shows a dominant peak below 3.5 Å, confirming chemisorption, with additional peaks beyond 3.5 Å reflecting physisorption. These results demonstrate that Q-22 achieves strong and stable adsorption, facilitating effective electron donation and acceptance at active sites, consistent with theoretical predictions, MD simulations, and experimental surface analyses [83].

Table 13. Molecular dynamic simulation outputs and descriptors of the studied neutral and protonated Q-22 molecule on the iron (1 1 1) surface.

Structures	Q-22	Q-22-H$^+$
Total energy	157.26	360.54
Adsorption energy	-543.38	-269.28
Rigid adsorption energy	-452.06	-8.14
Deformation energy	-121.32	-253.14
dE$_{ad}$/dNi	-543.38	-269.28

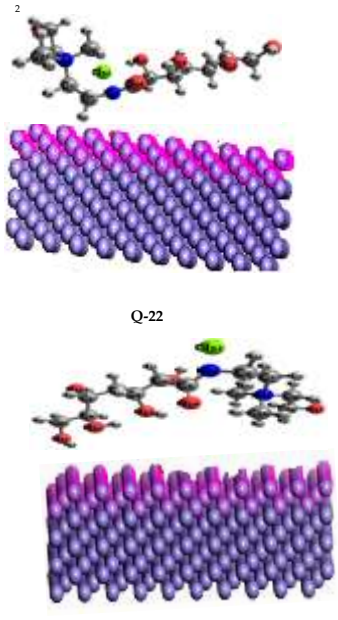

Q-22

Q-22-H$^+$

Side view

 doi:10.20944/preprints202602.1773.v1

Figure 18. Side views of the most stable adsorption configurations of the Q-22 and Q-22-H+ on the Fe (1 1 1) surface in the gas phase at 298 K.

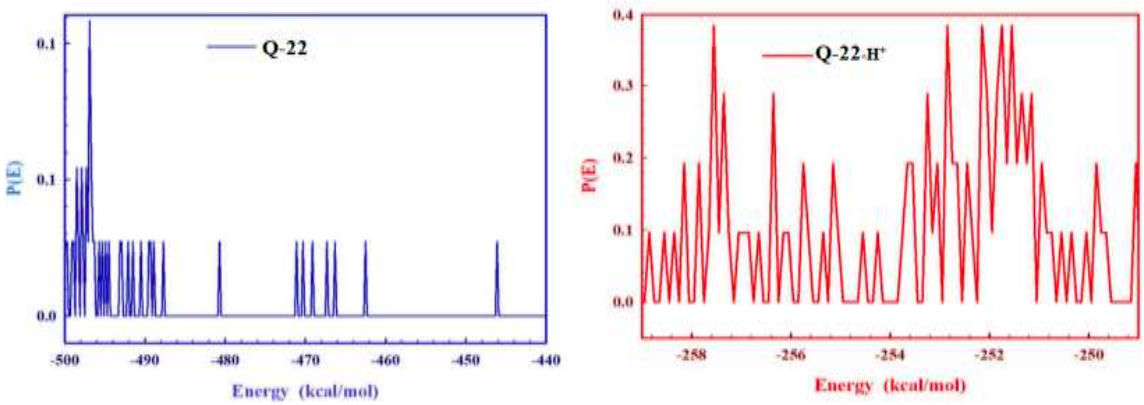

Figure 19. Adsorption energy distribution for the most suitable configuration of adsorption obtained for Q-22 and Q-22-H+ on the Fe (1 1 1) surface in the gas phase at 298 K.

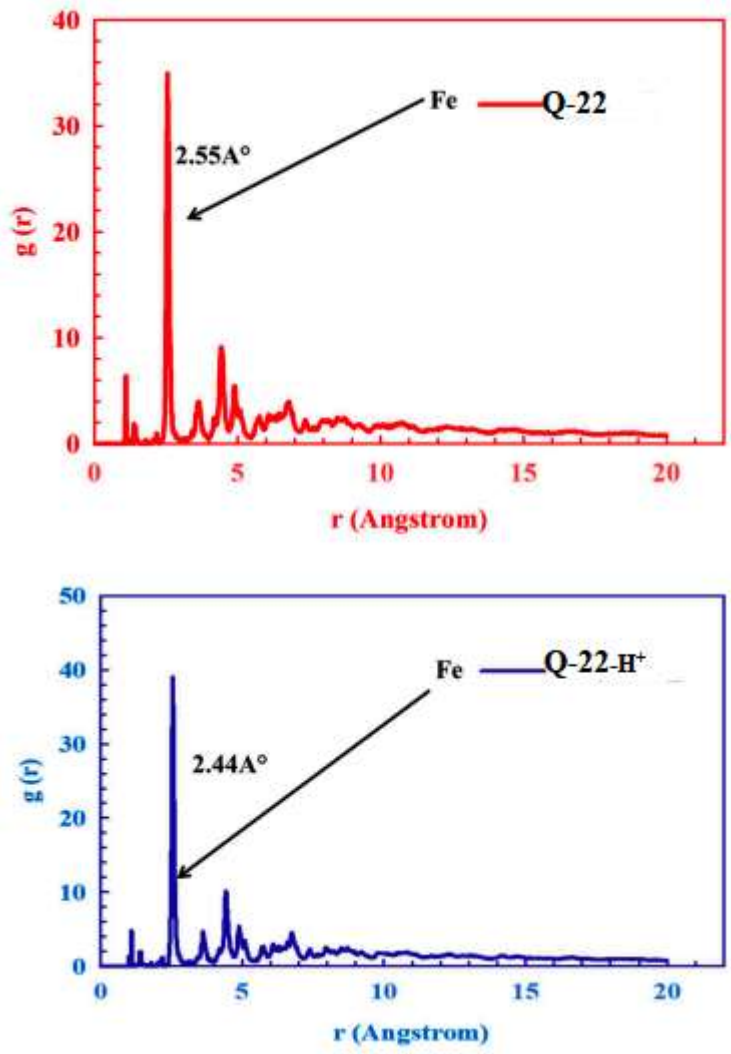

Figure 20. Radial distribution functions of adsorbed Q-22 and Q-22-H+ on the Fe (111) substrate by an adsorption locator mod.

 doi:10.20944/preprints202602.1773.v1

5. Conclusions

This comprehensive study demonstrates that Q-22 is an effective and potentially eco-benign corrosion inhibitor for CS in a 1.0 M HCl environment. The integration of gravimetric, electrochemical, surface morphological, and theoretical analyses leads to the following definitive conclusions:

1. Q-22 functions as an outstanding mixed-type corrosion inhibitor, achieving a maximum inhibition efficiency of **97.2%** at an optimal concentration of 277 μmol L^{-1}. Its performance is concentration-dependent, with efficiency increasing as the inhibitor dosage rises.
2. Electrochemical studies confirm that Q-22 adsorbs strongly onto the CS surface, leading to a substantial increase in charge transfer resistance (R_{ct}) and a marked reduction in double-layer capacitance (C_{dl}). These findings indicate the formation of a dense, adherent, and resistive protective film that impedes ionic and molecular transport to the metal surface.
3. Adsorption studies reveal that the inhibitor's adsorption on the steel surface is spontaneous and monolayer-forming, following the Langmuir adsorption isotherm. The calculated standard free energy of adsorption ($\Delta G° \approx -37$ kJ mol^{-1}) suggests that both physisorption and chemisorption contribute to the inhibition mechanism.
4. Thermodynamic analysis reveals that the presence of Q-22 substantially increases the apparent activation energy (Ea) of the corrosion process, indicating that the inhibitor raises the energy barrier for metal dissolution, primarily through a physisorption–chemisorption adsorption mechanism.
5. Direct visual evidence from SEM, AFM, and XPS analyses corroborates the electrochemical findings. The inhibited surface remains smooth and uniform, with a drastically reduced roughness (RMS = 30 nm) compared to the severely corroded, pitted surface in the blank acid (RMS = 200 nm), signifying the formation of a continuous and stable protective layer.
6. The experimental results and quantum chemical (DFT) and molecular modeling analyses, such as NBO and MD simulations, show that Q-22 has strong electron-donating and accepting capabilities that facilitate efficient adsorption on the metal surface and support the suggested inhibition mechanism.

In conclusion, Q-22 demonstrates outstanding inhibition efficiency for carbon steel corrosion in acidic environments through a spontaneous adsorption mechanism that produces a robust and adherent surface film. Its performance and molecular characteristics make it a promising candidate for use as a green corrosion inhibitor in industrial applications.

Author Contributions: Conceptualization, M.A., N.E., A.S.E., S.A.H. and M.A.M.I.; methodology, M.A. and S.A.H.; validation, M.A., N.E. and M.A.M.I.; formal analysis, N.E., A.S.E., and S.A.H.; investigation, M.A, N.E., A.S.E., and S.A.H.; resources, N.E., A.S.E., and S.A.H.; writing—original draft preparation, M.A., and M.A.M.I..; writing—review and editing, N.E., A.S.E., S.A.H. and M.A.M.I., supervision, M.A.M.I. and N.E. All authors have read and agreed to the published version of the manuscript.

Funding: This research received no external funding.

Data Availability Statement: All data generated or analyzed during this study are included in this published article.

Acknowledgments: The authors sincerely acknowledge the Department of Chemistry, Ain Shams University, for providing the research facilities and financial support necessary to complete this study.

Conflicts of Interest: The authors declare that they have no conflicts of interest.

References

1. Koch, G., Brongers, M., Thompson, N., Virmani, Y., & Payer, J. (2016). *International measures of prevention, application, and economics of corrosion technologies*. NACE International.

 doi:10.20944/preprints202602.1773.v1

2. Revie, R. W., & Uhlig, H. H. (2008). Corrosion and corrosion control: An introduction to corrosion science and engineering (4th ed.). John Wiley & Sons.
3. Roberge, P. R. (2008). Corrosion engineering: Principles and practice. McGraw-Hill.
4. Goyal, M., Kumar, S., Bahadur, I., Verma, C., & Ebenso, E. E. (2018). Organic corrosion inhibitors for industrial cleaning of ferrous and non-ferrous metals in acidic solutions: A review. *Journal of Molecular Liquids, 256*, 565–573. https://doi.org/10.1016/j.molliq.2018.02.045
5. Popoola, L. T., Grema, A. S., Latinwo, G. K., Gutti, B., & Balogun, A. S. (2013). Corrosion problems during oil and gas production and its mitigation. *Corrosion Reviews, 31*(3–6), 137–147. https://doi.org/10.1515/corrrev-2013-0011
6. Papavinasam, S. (2013). *Corrosion control in the oil and gas industry*. Gulf Professional Publishing. https://doi.org/10.1016/C2011-0-04556-7
7. Belhadi, M., Oubahou, M., Hammoudan, I., et al. (2024). A comprehensive assessment of carbon steel corrosion inhibition by 1,10-phenanthroline in the acidic environment: Insights from experimental and computational studies. *Environmental Science and Pollution Research, 31*(53), 62038–62055. https://doi.org/10.1007/s11356-024-36124-5
8. Rafique, M., Rafique, M. S., Akbar, R., & Quraishi, M. A. (2019). Integrated experimental and theoretical assessment of new pyrazole derivatives as corrosion inhibitors for mild steel in acidic medium. *Journal of Molecular Liquids, 276*, 101–112. https://doi.org/10.1016/j.molliq.2018.12.057
9. Afifi, M., Sliem, M. H., Elbasiony, N., Berdimurodov, E., Guo, L., El-Tabei, A. S., Ibrahim, M. A. M., & Abdullah, A. M. (2025). Adsorption mechanism and inhibition efficiency of Quaternium-15 (Q15) surfactant on carbon steel in 1 M HCl: A combined theoretical and experimental approach. *Results in Engineering, 28*, 106887. https://doi.org/10.1016/j.rineng.2025.106887
10. Khedr, B. M. A., Ramadan, S. K., Abdelkader, S. A., Abdelhamed, S., El-Etre, M. A., Elaraby, A., & Ibrahim, M. A. M. (2025). Multifaceted insights of experimental, surface, and computational investigations for synthesized carbon steel corrosion inhibitor based on pyrazolyl derivative in acidic environment. *Scientific Reports, 15*, 43246. https://doi.org/10.1038/s41598-025-28496-3
11. Omar, I. M. A., Elshamy, I. H., Abd El Halim, S., & Ibrahim, M. A. M. (2025). Electrochemical and computational analysis of thiocolchicoside as a new corrosion inhibitor for biomedical Ti6Al4V alloy in saline solution: DFT, NBO, and MD approaches. *Surfaces, 8*(4), 77. https://doi.org/10.3390/surfaces8040077
12. Abd El Rehim, S. S., Ibrahim, M. A. M., & Khaled, K. F. (1999). Corrosion inhibition and adsorption behaviour of 4-aminoantipyrine on mild steel in H_2SO_4. *Corrosion Prevention and Control, 46*(1), 30–38.
13. Ibrahim, M. A. M., Hamza, M. M., Ryl, J., Amin, M. A., & Abd El Rehim, S. S. (2021). The inhibition effect of eco-friendly sodium dodecyl sulfate on the corrosion behavior of SUS304L, SUS304H, and SUS316H stainless steels in sulfuric acid solution. *International Journal of Electrochemical Science, 16*(7), 1–15.
14. Singh, A., Ebenso, E. E., & Quraishi, M. A. (2021). Adsorption and corrosion inhibition behavior of polyethylene glycol and surfactants on mild steel in acidic media. *Journal of Molecular Liquids, 334*, 116495. https://doi.org/10.1016/j.molliq.2021.116495
15. Aslam, R., Mobin, M., Shoeb, M., & Zehra, S. (2021). Corrosion inhibition of steel using different families of chemical compounds: A review. *Journal of Molecular Liquids, 321*, 114888. https://doi.org/10.1016/j.molliq.2020.114888
16. Dehghani, A., Bahlakeh, G., & Ramezanzadeh, B. (2020). Green corrosion inhibitors for carbon steel in acidic environments: A review. *Journal of the Taiwan Institute of Chemical Engineers, 109*, 111–123. https://doi.org/10.1016/j.jtice.2020.02.007
17. Chigondo, M., & Chigondo, F. (2016). Recent natural corrosion inhibitors for mild steel: An overview. *Journal of Chemistry, 2016*, 6208937. https://doi.org/10.1155/2016/6208937
18. Tezel, Ü., & Guven, K. C. (2009). Biodegradation of quaternary ammonium compounds in environmental systems. *Environmental Toxicology and Pharmacology, 28*(3), 484–489. https://doi.org/10.1016/j.etap.2009.07.004
19. Abd El-Lateef, H. M. (2021). Experimental and computational investigation of novel cationic surfactants as corrosion inhibitors for carbon steel in HCl solution. *Journal of Industrial and Engineering Chemistry, 93*, 417–429. https://doi.org/10.1016/j.jiec.2020.10.037

 doi:10.20944/preprints202602.1773.v1

20. Fouda, A. S., El-Desouky, T. M., El-Badry, B. A., & El-Azzam, E. M. (2020). The role of some organic compounds as corrosion inhibitors for carbon steel in acidic medium: A comprehensive study. *Scientific Reports, 10*, 10476. https://doi.org/10.1038/s41598-020-67392-0
21. Hefnawy, A., Khaled, K. F., Abdelshafi, N. S., & Ibrahim, M. A. M. (2022). Eco-friendly corrosion inhibitors based on carbohydrate derivatives for carbon steel in acidic environments: A review. *Journal of Bio- and Tribo-Corrosion, 8*, 32. https://doi.org/10.1007/s40735-022-00620-1
22. El-Mokadem, T. H., Hashem, A. I., Abd El-Sattar, N. E. A., Dawood, E. A., & Abdelshafi, N. S. (2023). Green synthesis, electrochemical, DFT studies, and MD simulation of novel synthesized thiourea derivatives on carbon steel corrosion inhibition in 1.0 M HCl. *Journal of Molecular Structure, 1274*, 134567. https://doi.org/10.1016/j.molstruc.2022.134567
23. Abdelshafi, N. S., Farag, A. A., Heakal, F. E.-T., Badran, A.-S., Abdel-Azim, K. M., & Ibrahim, M. A. (2024). In-depth experimental assessment of two new aminocoumarin derivatives as corrosion inhibitors for carbon steel in HCl media combined with AFM, SEM/EDX, contact angle, and DFT/MD simulations. *Journal of Molecular Structure, 1304*, 137638. https://doi.org/10.1016/j.molstruc.2024.137638
24. Hadisaputra, S., Purwoko, A. A., Savalas, L. R. T., Prasetyo, N., & Yuanita, E. (2020). Quantum chemical and Monte Carlo simulation studies on inhibition performance of caffeine and its derivatives against corrosion of copper. *Coatings, 10*(11), 1086. https://doi.org/10.3390/coatings10111086
25. Arrousse, N., Salim, R., Kaddouri, Y., Zarrouk, A., Zahri, D., Hajjaji, F. E., Touzani, R., Taleb, M., & Jodeh, S. (2020). The inhibition behavior of two pyrimidine–pyrazole derivatives against corrosion in hydrochloric solution: Experimental, surface analysis, and in silico approach studies. *Arabian Journal of Chemistry, 13*(11), 5949–5967. https://doi.org/10.1016/j.arabjc.2020.04.030
26. Masroor, S., & Mobin, M. (2014). Non-ionic surfactant as corrosion inhibitor for aluminium in 1 M HCl and synergistic influence of gemini surfactant. *Chemical Science Review and Letters, 3*(10), 33–48.
27. Khaled, K. F. (2003). The inhibition of benzimidazole derivatives on corrosion of iron in 1 M HCl solutions. *Electrochimica Acta, 48*(17), 2493–2503. https://doi.org/10.1016/S0013-4686(03)00307-1
28. Pajkossy, T. (1994). Impedance of rough capacitive electrodes. *Journal of Electroanalytical Chemistry, 364*(1–2), 111–125. https://doi.org/10.1016/0022-0728(93)03185-5
29. Caprani, A., Epelboin, I., Morel, P., & Takenouti, H. (1975). Influence of anodic dissolution on the electrochemical impedance of iron in acidic sulfate medium. In *Proceedings of the 4th European Symposium on Corrosion Inhibitors* (pp. 571–583). University of Ferrara, Italy.
30. Bentiss, F., Traisnel, M., & Lagrenée, M. (2000). The substituted 1,3,4-oxadiazoles: A new class of corrosion inhibitors of mild steel in acidic media. *Corrosion Science, 42*(1), 127–146. https://doi.org/10.1016/S0010-938X(99)00049-9
31. Obot, I. B., Macdonald, D. D., & Gasem, Z. M. (2015). Density functional theory (DFT) as a powerful tool for the design of new organic corrosion inhibitors. Part 1: An overview. *Corrosion Science, 99*, 1–30. https://doi.org/10.1016/j.corsci.2015.01.037
32. Fouda, A. S., El-Askalany, A. H., & El-Habab, A. T. (2017). The role of some thiosemicarbazide derivatives as corrosion inhibitors for carbon steel in acidic media. *Journal of Molecular Liquids, 240*, 372–388. https://doi.org/10.1016/j.molliq.2017.05.108
33. Zhao, J., Duan, H., & Jiang, R. (2015). Synergistic corrosion inhibition effect of quinoline quaternary ammonium salt and gemini surfactant in H_2S and CO_2 saturated brine solution. *Corrosion Science, 91*, 108–119. https://doi.org/10.1016/j.corsci.2014.11.031
34. ASTM International. (2014). ASTM G3-14: Standard practice for conventions applicable to electrochemical measurements in corrosion testing. ASTM International. https://doi.org/10.1520/G0003-14
35. Zhang, J., Zhang, W., Liu, F., & Han, E.-H. (2022). Insight into the corrosion inhibition of novel macromolecular surfactants for carbon steel in acidic media. *Corrosion Science, 194*, 109941. https://doi.org/10.1016/j.corsci.2022.109941
36. El-Etre, A. Y. (2003). Inhibition of aluminum corrosion using *Opuntia* extract. *Corrosion Science, 45*(11), 2485–2495. https://doi.org/10.1016/S0010-938X(03)00066-0
37. McCafferty, E. (2010). *Introduction to corrosion science.* Springer. https://doi.org/10.1007/978-1-4419-0455-3

 doi:10.20944/preprints202602.1773.v1

38. Popova, A., Sokolova, E., Raicheva, S., & Christov, M. (2003). AC and DC study of the temperature effect on mild steel corrosion in acid media in the presence of benzimidazole derivatives. *Corrosion Science, 45*(1), 33–58. https://doi.org/10.1016/S0010-938X(02)00072-0
39. Lu, B. T., Chen, Z. K., Luo, J. L., Patchett, B. M., & Xu, Z. H. (2005). Pitting and stress corrosion cracking behavior in welded austenitic stainless steel. *Electrochimica Acta, 50*(6), 1391–1403. https://doi.org/10.1016/j.electacta.2004.07.045
40. Khamis, E., Ameen, M. A., Al-Andi, N. M., & Al-Senani, G. (2000). Effect of nonionic surfactant on the corrosion inhibition of aluminum in hydrochloric acid. *Corrosion, 56*(12), 127–135. https://doi.org/10.5006/1.3280543
41. Voudrias, E., Fytianos, F., & Bozani, E. (2002). Sorption–desorption isotherms of dyes from aqueous solutions and wastewaters with different sorbent materials. *Global Nest: The International Journal, 4*(1), 75–83.
42. Mohan, S., & Karthikeyan, J. (1997). Removal of lignin and tannin color from aqueous solution by adsorption onto activated carbon. *Environmental Pollution, 97*(1–2), 183–187. https://doi.org/10.1016/S0269-7491(97)00018-1
43. Djeddi, N., Benahmed, M., Akkal, S., Laouer, H., Makhloufi, E., & Gherraf, N. (2014). Chemical composition and antimicrobial activity of the essential oil of *Ruta montana L. Research on Chemical Intermediates, 41*(7), 4595–4605. https://doi.org/10.1007/s11164-014-1579-8
44. Deyab, M. A., & Abd El-Rehim, S. S. (2013). Effect of nonionic surfactant as an electrolyte additive on the performance of aluminum-air battery. *Journal of the Taiwan Institute of Chemical Engineers, 45*(4), 1065–1070. https://doi.org/10.1016/j.jtice.2013.10.004
45. Ali, S. A., El-Shareef, A. M., Al-Ghamdi, R. F., & Saeed, M. T. (2005). The isoxazolidines: The effects of steric factor and hydrophobic chain length on the corrosion inhibition of mild steel in acidic medium. *Corrosion Science, 47*(11), 2659–2678. https://doi.org/10.1016/j.corsci.2005.03.014
46. Seifzadeh, D., & Bezaatpour, A. (2013). A Schiff base compound as effective corrosion inhibitor for magnesium in acidic media. *Materials Chemistry and Physics, 138*(2–3), 794–802. https://doi.org/10.1016/j.matchemphys.2012.12.012
47. Mobin, M., & Rizvi, M. (2016). Inhibitory effect of xanthan gum and synergistic surfactant additives for mild steel corrosion in 1 M HCl. *Carbohydrate Polymers, 136*, 384–393. https://doi.org/10.1016/j.carbpol.2015.09.031
48. Eddy, N. O., & Ekop, A. S. (2007). Inhibition of the corrosion of mild steel in HCl by penicillin V potassium. *Materials Science Applications International Journal, 4*(1), 2008–2016.*
49. Saratha, R., Devi, S. S., Meenakshi, H. N., & Shyamala, R. (2011). Investigation of *Solanum nigrum* leaves extract as corrosion inhibitor for mild steel in acid medium. *International Journal of Current Research, 2*(1), 92–98.*
50. Hebrodike, M. M., Uroh, A. A., Okeoma, K. B., & Alozie, G. A. (2010). Inhibition of the corrosion of mild steel in HCl by *Vernonia amygdalina. African Journal of Pure and Applied Chemistry, 4*(8), 158–164.*
51. Hamdy, A., & El-Gendy, N. S. (2013). Thermodynamic, adsorption, and electrochemical studies for corrosion inhibition of carbon steel by henna extract in acid medium. *Egyptian Journal of Petroleum, 22*(1), 17–25. https://doi.org/10.1016/j.ejpe.2012.06.002
52. Ostovari, A., Hoseinieh, S. M., Peikari, M., Shadizadeh, S. R., & Hashemi, S. J. (2009). Corrosion inhibition of mild steel in 1 M HCl solution by henna extract: A comparative study of the inhibition by henna and its constituents (lawsone, gallic acid, α-D-glucose, and tannic acid). *Corrosion Science, 51*(9), 1935–1949. https://doi.org/10.1016/j.corsci.2009.05.024
53. Yadav, D. K., Maiti, B., & Quraishi, M. A. (2010). Electrochemical and quantum chemical studies of 3,4-dihydropyrimidin-2(1H)-ones as corrosion inhibitors for mild steel in hydrochloric acid solution. *Corrosion Science, 52*(11), 3586–3598. https://doi.org/10.1016/j.corsci.2010.07.017
54. Putilova, I. N., Balezin, S. A., & Barannik, V. P. (1960). *Metallic corrosion inhibitors.* Pergamon Press.
55. Tebbji, K., Faska, N., Tounsi, A., Oudda, H., Benkaddour, M., & Hammouti, B. (2007). The effect of some lactones as inhibitors for the corrosion of mild steel in 1 M hydrochloric acid. *Materials Chemistry and Physics, 106*(2–3), 260–267. https://doi.org/10.1016/j.matchemphys.2007.05.012

 doi:10.20944/preprints202602.1773.v1

56. Shukla, S. K., Quraishi, M. A., & Prakash, R. (2008). A self-doped conducting polymer "polyanthranilic acid": An efficient corrosion inhibitor for mild steel in acidic solution. *Corrosion Science, 50*(10), 2867–2872. https://doi.org/10.1016/j.corsci.2008.07.021
57. Zhang, J., Liu, J., Yu, W., Yan, Y., You, L., & Liu, L. (2015). Investigation of inhibition properties of sophorolipids for X65 steel corrosion in simulated oilfield produced water saturated with carbon dioxide. *Industrial & Engineering Chemistry Research, 54*(19), 5197–5203. https://doi.org/10.1021/ie504915n
58. Abd El-Rehim, S. S., Refaey, S. A. M., Taha, F., Saleh, M. B., & Ahmed, R. A. (2001). Corrosion inhibition of mild steel in acidic medium using 2-amino-thiophenol and 2-cyanomethyl-benzothiazole. *Journal of Applied Electrochemistry, 31*(4), 429–435. https://doi.org/10.1023/A:1017546512388
59. Finšgar, M., & Jackson, J. (2014). Application of corrosion inhibitors for steels in acidic media for the oil and gas industry: A review. *Corrosion Science, 86*, 17–41. https://doi.org/10.1016/j.corsci.2014.04.044
60. Verma, C., Ebenso, E. E., Bahadur, I., & Quraishi, M. A. (2018). An overview on plant extracts as environmentally sustainable and green corrosion inhibitors for metals and alloys in aggressive corrosive media. *Journal of Molecular Liquids, 266*, 577–590. https://doi.org/10.1016/j.molliq.2018.06.110
61. Quraishi, M. A., Singh, A., & Chauhan, D. S. (2022). Recent progress in surfactant-type corrosion inhibitors for metals in acidic media. *Journal of Molecular Liquids, 367*, 120505. https://doi.org/10.1016/j.molliq.2022.120505
62. Zheng, T., Zhang, Z., Zhao, X., Liu, Y., & Xu, X. (2022). Synergistic corrosion inhibition effects of quaternary ammonium salt cationic surfactants and thiourea on Q235 steel in sulfuric acid: Experimental and theoretical research. *Corrosion Science, 199*, 110199. https://doi.org/10.1016/j.corsci.2022.110199
63. Li, X., Deng, S., & Du, G. (2022). Nonionic surfactant of coconut diethanolamide as a novel corrosion inhibitor for cold-rolled steel in both HCl and H_2SO_4 solutions. *Journal of the Taiwan Institute of Chemical Engineers, 131*, 104171. https://doi.org/10.1016/j.jtice.2021.104171
64. Mobin, M., Aslam, J., & Alreface, S. H. (2022). An investigation on the synthesis, characterization and anti-corrosion properties of choline-based ionic liquids as novel and environmentally friendly inhibitors for mild steel corrosion in 5% HCl. *Journal of Colloid and Interface Science, 620*, 293–312. https://doi.org/10.1016/j.jcis.2022.04.049
65. Paiva, V. M., Silva, T. F., Falcão, S. G., Rocha, C., & Villamil, R. F. (2024). Novel eco-friendly green inhibitor of corrosion based on acerola (*Malpighia glabra*) waste aqueous extract for mild steel in 1 mol L^{-1} HCl solution. *Surfaces and Interfaces, 47*, 104187. https://doi.org/10.1016/j.surfin.2024.104187
66. El-Etre, A. Y., Abdallah, M., & El-Tantawy, Z. E. (2008). The adsorption behavior of some thiosemicarbazide derivatives on mild steel in acidic medium. *Corrosion Science, 50*(5), 1465–1471. https://doi.org/10.1016/j.corsci.2008.01.020
67. Oguzie, E. E., Li, Y., Wang, F., & Wang, S. G. (2009). Understanding corrosion inhibition mechanisms through surface analysis and quantum chemical calculations: A review. *The Journal of Physical Chemistry C, 113*(19), 8420–8429. https://doi.org/10.1021/jp8097685
68. Zhang, D., Wang, Y., Liu, L., & Wei, Y. (2022). Insight into the anti-corrosion performance of a novel hydrophobic film constructed on copper surface. *Corrosion Science, 194*, 109941. https://doi.org/10.1016/j.corsci.2022.109941
69. He, T., Ma, H., Wang, Y., & Zhang, Y. (2020). Construction of a superhydrophobic surface on AZ31B magnesium alloy for corrosion protection. *Surface and Coatings Technology, 385*, 125429. https://doi.org/10.1016/j.surfcoat.2020.125429
70. Ramezanzadeh, B., Bahlakeh, G., & Ramezanzadeh, M. (2018). Study of the effect of a new eco-friendly surface treatment on the corrosion resistance of mild steel in HCl solution. *Journal of the Taiwan Institute of Chemical Engineers, 91*, 439–455. https://doi.org/10.1016/j.jtice.2018.06.004
71. Ye, Y., Zhang, D., Li, J., Liu, T., Wang, J., & Wang, Y. (2021). One-step fabrication of a superhydrophobic surface for corrosion protection of aluminum alloy. *Colloids and Surfaces A: Physicochemical and Engineering Aspects, 612*, 125991. https://doi.org/10.1016/j.colsurfa.2020.125991
72. Radwan, A. B., Ibrahim, M. A., Ismail, E. H., & Santo, L. (2025). Beyond wetting: Unveiling the theoretical and practical power of superhydrophobic coatings in multifunctional applications. *Industrial & Engineering Chemistry Research.* Advance online publication. https://doi.org/10.1021/acs.iecr.4c03665

 doi:10.20944/preprints202602.1773.v1

73. Khaled, K. F., Hamed, M. N. H., Abdel-Azim, K. M., & Abdelshafi, N. S. (2011). Inhibition of copper corrosion in 3.5% NaCl solutions by a new pyrimidine derivative: Electrochemical and computer simulation techniques. *Journal of Solid State Electrochemistry, 15*(4), 663–675. https://doi.org/10.1007/s10008-010-1110-0
74. Zuo, X., Li, W., Luo, W., Zhang, X., Qiang, Y., Zhang, J., Li, H., & Tan, B. (2021). Research of *Lilium brownii* leaves extract as a commendable and green inhibitor for X70 steel corrosion in hydrochloric acid. *Journal of Molecular Liquids, 321*, 114914. https://doi.org/10.1016/j.molliq.2020.114914
75. Zarrouk, A., El Ouali, I., Bouachrine, M., Hammouti, B., Ramli, Y., Essassi, E. M., Warad, I., Aouniti, A., & Salghi, R. (2013). Theoretical approach to the corrosion inhibition efficiency of some quinoxaline derivatives of steel in acid media using the DFT method. *Research on Chemical Intermediates, 39*(3), 1125–1136. https://doi.org/10.1007/s11164-012-0671-1
76. Saady, A., Rais, Z., Benhiba, F., Salim, R., Ismaily Alaoui, K., Arrousse, N., Elhajjaji, F., Taleb, M., Jarmoni, K., Kandri Rodi, Y., Warad, I., & Zarrouk, A. (2021). Chemical, electrochemical, quantum, and surface analysis evaluation on the inhibition performance of novel imidazo[4,5-b]pyridine derivatives against mild steel corrosion. *Corrosion Science, 189*, 109621. https://doi.org/10.1016/j.corsci.2021.109621
77. Laabaissi, T., Benhiba, F., Rouifi, Z., Missioui, M., Ourrak, K., Oudda, H., Ramli, Y., Warad, I., Allali, M., & Zarrouk, A. (2019). New quinoxaline derivative as a green corrosion inhibitor for mild steel in mild acidic medium: Electrochemical and theoretical studies. *International Journal of Corrosion and Scale Inhibition, 8*(2), 241–258. https://doi.org/10.17675/2305-6894-2019-8-2-6
78. Gece, G., & Bilgiç, S. (2010). A theoretical study on the inhibition efficiencies of some amino acids as corrosion inhibitors of nickel. *Corrosion Science, 52*(10), 3435–3443. https://doi.org/10.1016/j.corsci.2010.06.015
79. Wang, H., Wang, X., Wang, H., Wang, L., & Liu, A. (2007). DFT study of new bipyrazole derivatives and their potential activity as corrosion inhibitors. *Journal of Molecular Modeling, 13*(2), 147–153. https://doi.org/10.1007/s00894-006-0135-x
80. Rbaa, M., & Lakhrissi, B. (2019). Novel oxazole and imidazole based on 8-hydroxyquinoline as corrosion inhibitors of mild steel in HCl solution: Insights from experimental and computational studies. *Surfaces and Interfaces, 15*, 43–51. https://doi.org/10.1016/j.surfin.2019.01.010
81. El-Deeb, M. M., Abdel-Shafi, N. S., & Shamroukh, A. H. (2018). Electrochemical, DFT and Monte Carlo simulations studies to evaluate the inhibition effect of novel pyridazine derivatives on iron pitting corrosion in 3.5% NaCl. *International Journal of Electrochemical Science, 13*, 5352–5371. https://doi.org/10.20964/2018.06.070
82. Abdelsalam, M. M., Bedair, M. A., Hassan, A. M., Heakal, B. H., Younis, A., Elbialy, Z. I., Badawy, M. A., Fawzy, H. E.-D., & Fareed, S. A. (2022). Green synthesis, electrochemical, and DFT studies on the corrosion inhibition of steel by some novel triazole Schiff base derivatives in hydrochloric acid solution. *Arabian Journal of Chemistry, 15*, 103491. https://doi.org/10.1016/j.arabjc.2021.103491
83. Abdelshafi, N. S., Ibrahim, M. A., Badran, A.-S., & Halim, S. A. (2022). Experimental and theoretical evaluation of a newly synthesized quinoline derivative as corrosion inhibitor for iron in 1.0 M hydrochloric acid solution. *Journal of Molecular Structure, 1250*, 131750. https://doi.org/10.1016/j.molstruc.2021.131750
84. Belghiti, M. E., Echihi, S., Dafali, A., Karzazi, Y., Bakasse, M., Elalaoui-Elabdallaoui, H., Olasunkanmi, L. O., Ebenso, E. E., & Tabyaoui, M. (2019). Computational simulation and statistical analysis on the relationship between corrosion inhibition efficiency and molecular structure of some hydrazine derivatives in phosphoric acid on mild steel surface. *Applied Surface Science, 491*, 707–722. https://doi.org/10.1016/j.apsusc.2019.04.125
85. Cao, Z., Tang, Y., Cang, H., Xu, J., Lu, G., & Jing, W. (2014). Novel benzimidazole derivatives as corrosion inhibitors of mild steel in the acidic media. Part II: Theoretical studies. *Corrosion Science, 83*, 292–298. https://doi.org/10.1016/j.corsci.2014.02.025
86. Politzer, P., & Murray, J. S. (2002). The fundamental nature and role of the electrostatic potential in atoms and molecules. *Theoretical Chemistry Accounts, 108*(3), 134–142. https://doi.org/10.1007/s00214-002-0363-9
87. Abd El-Lateef, H. M., Sayed, A. R., Gomha, S. M., Bakir, E. M., & Shalabi, K. (2021). Synthesis and study of poly[(hydrazinylazo)]thiazoles as potent corrosion inhibitors for cast iron–carbon alloy in molar HCl: A

 doi:10.20944/preprints202602.1773.v1

collective computational and experiential methods approach. *Journal of Molecular Liquids, 337*, 116555. https://doi.org/10.1016/j.molliq.2021.116555

88. Fouda, A., Ismail, M., Abousalem, A. S., & Elewady, G. (2017). Experimental and theoretical studies on corrosion inhibition of 4-amidinophenyl-2,2′-bifuran and its analogues in acidic media. *RSC Advances, 7*(73), 46414–46430. https://doi.org/10.1039/C7RA08092A
89. Mert, B. D., Yüce, A. O., Kardaş, G., & Yazıcı, B. (2014). Inhibition effect of 2-amino-4-methylpyridine on mild steel corrosion: Experimental and theoretical investigation. *Corrosion Science, 85*, 287–295. https://doi.org/10.1016/j.corsci.2014.04.032
90. Guerrab, W., Chung, I.-M., Kansiz, S., Mague, J. T., Dege, N., Taoufik, J., Salghi, R., Ali, I. H., Khan, M. I., & Lgaz, H. (2019). Synthesis, structural and molecular characterization of 2,2-diphenyl-2H,3H,5H,6H,7H-imidazo[2,1-b][1,3]thiazin-3-one. *Journal of Molecular Structure, 1197*, 369–376. https://doi.org/10.1016/j.molstruc.2019.07.081
91. Guerrab, W., Lgaz, H., Kansiz, S., Mague, J. T., Dege, N., Ansar, M., Marzouki, R., Taoufik, J., Ali, I. H., & Chung, I.-M. (2020). Synthesis of a novel phenytoin derivative: Crystal structure, Hirshfeld surface analysis, and DFT calculations. *Journal of Molecular Structure, 1205*, 127630. https://doi.org/10.1016/j.molstruc.2019.127630
92. Abdallah, M., Al Bahir, A., Altass, H. M., Fawzy, A., El Guesmi, N., Al-Gorair, A. S., Benhiba, F., Warad, I., & Zarrouk, A. (2021). Anticorrosion and adsorption performance of expired antibacterial drugs on Sabic iron corrosion in HCl solution: Chemical, electrochemical, and theoretical approach. *Journal of Molecular Liquids, 330*, 115702. https://doi.org/10.1016/j.molliq.2021.115702